

# Candidate strongly-lensed Type Ia supernovae in the Zwicky Transient Facility archive

A. Townsend<sup>1,\*</sup>, J. Nordin<sup>1</sup>, A. Sagués Carracedo<sup>2</sup>, M. Kowalski<sup>1,3</sup>, N. Arendse<sup>2</sup>, S. Dhawan<sup>4</sup>,  
A. Goobar<sup>2</sup>, J. Johansson<sup>2</sup>, E. Mörtzell<sup>2</sup>, S. Schulze<sup>5</sup>, I. Andreoni<sup>6,7,8</sup>, E. Fernández<sup>9</sup>, A. G. Kim<sup>10</sup>,  
P. E. Nugent<sup>10,11</sup>, F. Prada<sup>9</sup>, M. Rigault<sup>12</sup>, N. Sarin<sup>2,13</sup>, D. Sharma<sup>11</sup>, E. C. Bellm<sup>14</sup>, M. W. Coughlin<sup>15</sup>,  
R. Dekany<sup>16</sup>, S. L. Groom<sup>17</sup>, L. Lacroix<sup>2,18</sup>, R. R. Laher<sup>17</sup>, R. Riddle<sup>17</sup>, J. Aguilar<sup>10</sup>, S. Ahlen<sup>19</sup>,  
S. Bailey<sup>10</sup>, D. Brooks<sup>20</sup>, T. Claybaugh<sup>11</sup>, A. de la Macorra<sup>21</sup>, A. Dey<sup>22</sup>, B. Dey<sup>23</sup>, P. Doel<sup>20</sup>, K. Fanning<sup>24,25</sup>,  
J. E. Forero-Romero<sup>26,27</sup>, E. Gaztañaga<sup>28,29,30</sup>, S. Gontcho A Gontcho<sup>10</sup>, K. Honscheid<sup>31,32,33</sup>, C. Howlett<sup>34</sup>,  
T. Kisner<sup>10</sup>, A. Kremin<sup>10</sup>, A. Lambert<sup>10</sup>, M. Landriau<sup>10</sup>, L. Le Guillou<sup>18</sup>, M. E. Levi<sup>10</sup>, M. Manera<sup>35,36</sup>,  
A. Meisner<sup>22</sup>, R. Miquel<sup>36,37</sup>, J. Moustakas<sup>38</sup>, E. Mueller<sup>39</sup>, A. D. Myers<sup>40</sup>, J. Nie<sup>41</sup>,  
N. Palanque-Delabrouille<sup>10,42</sup>, C. Poppett<sup>10,11,43</sup>, M. Rezaie<sup>44</sup>, G. Rossi<sup>45</sup>, E. Sanchez<sup>46</sup>, D. Schlegel<sup>10</sup>,  
M. Schubnell<sup>47,48</sup>, H. Seo<sup>49</sup>, D. Sprayberry<sup>22</sup>, G. Tarlé<sup>48</sup>, and H. Zou<sup>41</sup>

(Affiliations can be found after the references)

Received — XX, XXXX; accepted — XX, XXXX

## ABSTRACT

**Context.** Gravitationally lensed Type Ia supernovae (gISNe Ia) are unique astronomical tools that can be used to study cosmological parameters, distributions of dark matter, as well as the astrophysics of the supernovae and the intervening lensing galaxies themselves. A small number of highly magnified gISNe Ia have been discovered by ground-based telescopes, such as the Zwicky Transient Facility (ZTF), but simulations predict that a fainter, undetected population may also exist.

**Aims.** We present a systematic search for gISNe Ia in the ZTF archive of alerts distributed from 1 June 2019 to 1 September 2022.

**Methods.** Using the AMPEL platform, we developed a pipeline that distinguishes candidate gISNe Ia from other variable sources. Initial cuts were applied to the ZTF alert photometry (with constraints on the peak absolute magnitude and the distance to a catalogue-matched galaxy, as examples) before forced photometry was obtained for the remaining candidates. Additional cuts were applied to narrow down the candidates further, based on their light curve colours, lens galaxy colours, and the resulting parameters from fits to the SALT2 SN Ia template. Candidates were also cross-matched with the DESI spectroscopic catalogue.

**Results.** Seven transients were identified that passed all the cuts and had an associated galaxy DESI redshift, which we present as gISNe Ia candidates. While superluminous supernovae (SLSNe) cannot be fully rejected as sources, two events, ZTF19abpjcim and ZTF22aahmovu, are significantly different from typical SLSNe and their light curves can be modelled as two-image gISNe Ia systems. From this two-image modelling, we estimate time delays of  $22 \pm 3$  and  $34 \pm 1$  days for the two events, respectively, which suggests that we have uncovered a population of gISNe Ia with longer time delays.

**Conclusions.** The pipeline presented is both efficient and sensitive enough to parse full alert streams from optical observatories. It is currently being applied to the live ZTF alert stream so that future candidates can be identified while active and follow-up observations can be initiated. This pipeline could be the foundation for gISNe Ia searches in future surveys, such as the Vera C. Rubin Observatory's Legacy Survey of Space and Time.

**Key words.** supernovae: general – gravitational lensing: strong – methods: observational – techniques: photometric

## 1. Introduction

Strong gravitational lensing is a consequence of general relativity, where light from a distant source is deflected and magnified due to the mass of an intervening object. The intervening massive object is the lens, and it acts like a gravitational telescope to observe the high-redshift universe. Over the last few decades, there have been many observations of strongly-lensed galaxies and quasars, but a rapidly developing area of research is the observation of lensed transients. Type Ia supernovae (SNe Ia), the explosions of white dwarf stars in binary star systems, are bright, standardisable candles. Therefore, strongly-lensed Type Ia supernovae (gISNe Ia) are extremely valuable astrophysical tools.

In terms of supernova physics, gISNe Ia allow us to probe distant SNe Ia and study their redshift evolution (Petrushevskaya et al. 2017; Johansson et al. 2021). This is important to verify that high-redshift SNe Ia are standardisable and can be included in the Hubble diagram. In terms of lensing physics, gISNe Ia can be used to determine the matter distribution in lensing systems. Additionally, from the recent discovery of SN Zwicky (Goobar et al. 2023), the authors suggested that gISNe Ia could be vital for the study of previously unknown compact lens systems. In terms of cosmology, gISNe Ia can be utilised in the method of time-delay cosmography to measure the Hubble constant ( $H_0$ ), which was first proposed by Refsdal (1964). Strong lensing produces multiple images of the supernova explosion, which travel different paths with different gravitational potentials to reach the observer, leading to time delays between the images. From mea-

\* Email: alice.townsend@physik.hu-berlin.de

measurements of the time delays and a model of the lens galaxy’s gravitational potential, an absolute distance (known as the ‘time-delay distance’) for the system can be determined. This distance provides constraints on  $H_0$  and, to a lesser degree, the mass density parameter,  $\Omega_M$ , and the dark energy equation of state,  $w(z)$  (Goobar et al. 2002).

The method of time-delay cosmography has previously been employed with quasar sources (e.g. Wong et al. 2020; Shajib et al. 2020; Millon et al. 2020). One of the benefits of using time-delay cosmography with gISNe Ia is that SNe Ia are standardisable candles, with a known peak absolute magnitude that provides absolute magnification constraints. This allows us to constrain the mass-sheet degeneracy (Falco et al. 1985), which is a systematic effect where one allows for the addition of a constant surface mass density to the lens system, resulting in a degeneracy where all of the lensing observables remain unchanged, except for the time delays. This degeneracy can be broken by knowledge of the unlensed apparent brightness (Birrer et al. 2022). Another benefit is that SNe Ia have predictable light curve shapes with a duration of  $\sim 30$  days, whereas the timescale required to monitor time delays from lensed quasars is several years due to their stochastic variability. Additionally, the host and lens galaxy can be studied without any contamination from the supernova once it has faded, which is not always possible for lensed quasars.

At the time of publication, only three gISNe Ia have been detected with ground-based telescopes: PS1-10afx with the Panoramic Survey Telescope and Rapid Response System (Pan-STARRS; Chornock et al. 2013; Quimby et al. 2013), iPTF16geu with the Intermediate Palomar Transient Factory (iPTF; Goobar et al. 2017), and SN Zwicky with the Zwicky Transient Facility (ZTF; Goobar et al. 2023; Pierel et al. 2023). All of these events experienced a high magnification (with a total magnification factor,  $\mu$ , of greater than 20) allowing them to be followed up and classified by surveys that obtain spectra of nearby transients. This implies that a larger sample of less magnified gISNe Ia could exist, which may have already been observed by surveys such as ZTF, but remain undiscovered because they would not be targeted by spectroscopic follow-up programs. Additionally, with upcoming large-scale optical surveys such as the Vera C. Rubin Observatory’s Legacy Survey of Space and Time (LSST; Ivezić et al. 2019), it is necessary for us to develop a systematic approach for detecting all gISNe Ia, instead of discovering only the extremely luminous objects. Most transients found by LSST will be too faint to be observable, even with 8 m-class telescopes. Thus, with the lack of spectroscopic follow-up resources available, it would be valuable to devise a method to identify candidate gISNe Ia before a spectrum of the transient is obtained.

In this work, we present a systematic search of the ZTF archive for gISNe Ia. We developed a pipeline that is capable of filtering alerts and distinguishing candidate gISNe Ia from other variable sources. Initial cuts were applied to the ZTF alert photometry (e.g. constraints on peak absolute magnitude) before forced photometry was obtained for the remaining candidates. Additional cuts were applied to the remaining candidates based on their light curve colours, lens galaxy colours, and parameters from light curve fits. We also cross-matched the candidates to the Dark Energy Spectroscopic Instrument (DESI) survey catalogue.

The structure of this article is as follows. Section 2 discusses the methods previously employed to search for lensed supernovae, how these methods were used as guidelines when implementing the search pipeline, and predictions for what we should expect to find in the ZTF archive. The data from ZTF used in this analysis is summarised in Sect. 3.1. Section 3.2 outlines the

real-time alert processing platform AMPEL, which allowed us to analyse the ZTF data and structure our pipeline. In Sect. 4, we describe our method to identify probable gISNe Ia, starting with the initial alert pipeline described in Sect. 4.1. The candidates remaining after the initial selection method were analysed in parallel in Sect. 4.2, where we cross-match to the DESI spectroscopic catalogue, and Sect. 4.3, where we continue to filter the candidates based on more restrictive cuts. Section 4.4 summarises the sample of candidates that were selected by the two methods. In Sect. 5, we report on the properties of this sample by discussing the possible contaminants (Sect. 5.1) and by comparing to the Bright Transient Survey (Sect. 5.2) and to previously observed gISNe Ia (Sect. 5.3). Our seven most likely candidates (labelled the ‘gold sample’) are analysed in more detail in Section 6. The two objects we present as likely gISNe Ia, ZTF19abpjjcm and ZTF22aahmovu, are examined in Sects. 6.4.1 and 6.4.2, respectively. Finally, in Sect. 7, we elucidate the findings of our study and what further work is required to confirm that our candidates are truly gISNe Ia.

## 2. Strategy for detecting lensed supernovae

The strategy for finding lensed supernovae depends on whether the instrument used is capable of resolving the individual images. Lensed supernovae discovered from spatially resolved data include SN Refsdal (Type II, Kelly et al. 2015) and SN Requiem (Type Ia, Rodney et al. 2021), which were both recovered from Hubble Space Telescope (HST) data that distinguished the separate images of each SN. More recently, the James Webb Space Telescope (JWST) discovered the triply-imaged Type Ia SN H0pe (Frye et al. 2023).

To detect unresolved lensed supernovae, a variety of strategies can be employed. Goldstein & Nugent (2017) put forward the idea of searching for magnified sources (with a peak  $B$ -band absolute magnitude greater than the typical  $-19.4$  mag for SNe Ia) close to elliptical galaxies. Their reasoning is that normal SNe Ia are the brightest objects in quiescent galaxies, so there is a high likelihood that the magnified object is a lensed transient from a background galaxy. Wojtak et al. (2019) calculated gISNe discovery rates as a function of survey depth and found that shallower, pre-LSST surveys such as ZTF would not be able to detect any multiple images from gISNe Ia. Instead, the only viable method would be to find magnified sources as suggested by Goldstein & Nugent (2017).

Other methods proposed include detection from light curve information alone (Bag et al. 2021; Denissenya et al. 2022), monitoring known galaxy-galaxy strong-lens systems (Shu et al. 2018; Craig et al. 2021), or known cluster systems (Saini et al. 2000; Sullivan et al. 2000). However, these methods are not utilised in our following analysis. Firstly, we would struggle to characterise gISNe Ia from light curves alone due to occasional gaps in the light curve and limited filters (usually the  $g$ - and  $r$ -bands are available, whereas the  $i$ -band is limited in ZTF), so instead we must combine the parameters we extract from the light curve with additional information (e.g. from a catalogue-matched lens/host galaxy). Secondly, the three gISNe Ia discovered by ground-based telescopes had lens galaxies that were previously unknown, as they were compact (with an Einstein radius,  $\theta_E$ , of less than 0.5 arcseconds) and could not be detected from ground-based galaxy surveys. Therefore, monitoring known galaxy-galaxy strong-lens systems might not be the optimal search method as it would bias the sample to massive lenses. Thirdly, monitoring cluster systems with shallow ground-based surveys has so far only been successful with the discovery of

weakly lensed supernovae (e.g. Goobar et al. 2009; Patel et al. 2014; Nordin et al. 2014; Rodney et al. 2015; Petrushevska et al. 2016), which are not the focus of this work.

Quimby et al. (2014) were the first to suggest using light curve colours as a metric for distinguishing lensed supernovae from unlensed. Specifically, they proposed that the observed  $r - i$  vs.  $i$ -band distribution at peak magnitude for PS1-10afx (the gISNe Ia detected by Pan-STARRS) differed significantly from the distributions of unlensed SNe. We expect gISNe to be observed at higher redshifts (due to the probability of lensing and the number of SNe increasing with redshift) and, as a result, they will be redder than nearby, unlensed SNe at similar apparent magnitudes (Quimby et al. 2014). This concept is also demonstrated in simulations by Sagués Carracedo et al. (in prep.), which we will hereafter refer to as SC24. By generating realistic light curves from SNe Ia templates, the authors of SC24 show how the distributions of  $g - r$ ,  $g - i$ , and  $r - i$  at different light curve epochs differ for lensed and unlensed SNe Ia.

In SC24, the authors examine the sample of gISNe Ia that would have been detected by ZTF specifically, by incorporating the observing logs for ZTF, so the results can be directly applied to our systematic search. The findings of SC24 formed a part of our pipeline; in particular, the light curve colours discussed above, but also the simulated distributions of host and lens redshifts. From the distributions of the host and lens galaxy redshifts in SC24, we do not expect to find any gISNe Ia in host galaxies in the range  $z > 0.1$ . Additionally, less than 3% of identifiable gISNe have lens galaxies in the range  $z > 0.1$ .

SC24 also performed SALT2 light curve fits to simulated gISNe Ia light curves. The SALT2 model is a light curve template for SNe Ia based on two observable parameters: the stretch,  $x_1$ , and the colour,  $c$ . This model is based on empirical observations, because of the current lack of understanding about SN Ia progenitor explosions (Guy et al. 2007). For typical SNe Ia (e.g. the ones that are used in cosmological analyses), we expect  $x_1$  values between  $-3$  and  $3$ , and  $c$  values between  $-0.5$  and  $1$ . As shown in SC24, simulated gISNe Ia display a wider distribution of stretch values (approximately  $-3 \lesssim x_1 \lesssim 10$ ) and are redder in colour ( $c \gtrsim 0$ ). They demonstrate that a cut of  $c > 0$  removes approximately half of the unlensed SNe Ia sample and most of the lensed core-collapse supernova contaminants, whilst also retaining 90% of the gISNe Ia sample. SC24 also determined the peak  $B$ -band absolute magnitude distribution from the SALT2 fits, assuming the redshift of the lens galaxy is the supernova redshift (the motivation behind this assumption will be explained in Sect. 4.1). They show that we can exclude almost all unlensed SNe Ia with a cut of  $M_B > -20$  mag, although this removes approximately 20% of the gISNe Ia sample.

In addition to the simulations of SC24, our pipeline utilised a relationship between  $x_1$  and peak brightness (or, alternatively, magnification) for gISNe Ia. Recall that light curves from lensed transients are the sum of the individual, unresolved images. Therefore, we expect that objects with shorter time delays will have narrower light curves (meaning smaller  $x_1$  values) with greater peak brightness (and thus, greater total magnification). This is because the peak values of the individual images will be observed at approximately the same observation epoch, since the time difference between the arrival of each image is small. Additionally, the time delays and magnifications in a lensing system are negatively correlated. Conversely, we expect that objects with longer time delays will have wider light curves (larger  $x_1$  values) with lower magnifications. This relationship between  $x_1$  and magnification was implemented in our methodology to be sensitive to objects with both short and long time delays.

The most challenging part of an archival study is estimating the true brightness of the candidates in the sample. Our analysis pipeline allowed us to process and filter the entire ZTF alert stream, which was necessary to consider faint, unclassified transients that have not been studied previously. Because we did not have spectra for these unclassified transients, we utilised the redshifts from catalogue-matched nearby galaxies (which, in the case of an actual lensed supernova, would likely be the lensing galaxy). Current spectroscopic surveys are limited to brighter, lower redshift galaxies, meaning that we rely on photometric redshift estimates for distant galaxies, which have larger uncertainties but are more complete. In previous work by Magee et al. (2023), the authors performed a similar archival search for lensed supernovae from the sample of transients that were observed by ZTF and reported to the Transient Name Server (TNS). However, this public sample was limited to brighter objects that would have been reported by the ZTF brokers, and the analysis of the transients did not utilise ZTF forced photometry to study objects at deeper magnitudes.

Several studies have forecasted the rates of gravitationally lensed supernovae that ZTF would find per year. For example, in a study by Goldstein et al. (2019), the authors predicted a discovery rate of 1.23 gISNe Ia per year and at least 7.37 other types of supernovae per year. Therefore, across the 3.25 years in this archival search, we expect there to be approximately 28 gISNe in our sample, with 4 of those being SNe Ia. However, Goldstein et al. (2019) assumed that observations taken in the same filter in a single night would be stacked, whereas our analysis utilises forced photometry data instead. Additionally, Wojtak et al. (2019) predicted that ZTF would observe approximately two gISNe Ia per year (meaning that there should be 6 or 7 total objects in our sample). More conservatively, Sainz de Murieta et al. (2023) forecasted that ZTF should have observed roughly 0.2 gISNe Ia per year, which is consistent with SN Zwicky being the only discovery. However, when incorporating the ZTF observing logs, SC24 predicted that ZTF would detect gISNe Ia with at least five 5-sigma detections around the peak at a rate of approximately 4 per year. After requiring that the object is measured as over-luminous (assuming the object is at the lens redshift), the simulations of SC24 predict that approximately 1.4 gISNe Ia per year will remain. As a result of this study, we can expect to find up to 4 archival candidates in our analysis.

### 3. Analysing ZTF data using AMPEL

#### 3.1. The ZTF archive

The Zwicky Transient Facility is a wide-field, optical survey for time-domain astronomy (Bellm et al. 2019b; Graham et al. 2019). The survey utilises a camera with a field of view of 47 degrees squared on the Palomar 48-inch (P48) Telescope that observes in three filters ( $g$ -,  $r$ - and  $i$ -bands) (Dekany et al. 2020). The observation plan consists of a public survey in  $g$ - and  $r$ -band that scans the northern sky every two days and a partnership survey with a higher cadence and additional  $i$ -band photometry over a smaller region of the sky (Bellm et al. 2019a). In this study, we had access to both public and partnership data. On average, ZTF produces between 600,000 and 1.2 million alerts on a complete night of observation (Masci et al. 2019; Patterson et al. 2019).

Owing to the rapid scanning and extensive sky coverage of the survey, ZTF is an excellent precursor to LSST and is capable of detecting rare transients such as lensed supernovae. The Bright Transient Survey (BTS, Fremling et al. 2020; Perley et al. 2020) is a spectroscopic survey within ZTF that aims to acquire

spectra of all transients brighter than 18.5 magnitudes, which constitute the vast majority of classified objects in ZTF. Previously observed gISNe Ia may be unclassified in the ZTF archive, in particular, if they were significantly less magnified than discoveries such as SN Zwicky. Therefore, a systematic search of the ZTF archive is a promising avenue to identify less magnified gISNe Ia.

In this analysis, we have demonstrated a method to systematically identify probable unresolved gISNe Ia, by reducing a total of 98 567 163 unique alerts in ZTF between 1 June 2019 and 1 September 2022 to a sample of seven gISN Ia candidates. This approach will also be utilised in the final months of ZTF for a live search for lensed transients.

### 3.2. The AMPEL platform: alert processing and catalogue-matching

To systematically process all of the archival ZTF data, we require a platform that can ingest and filter large data sets. We also require the ability to cross-match our large sample of alerts to various photometric and spectroscopic redshift catalogues, so that we can estimate the redshift of each transient’s lens/host galaxy. To fulfil these objectives, we used AMPEL<sup>1</sup>, which is a publicly available real-time alert processing platform developed by Nordin et al. (2019). As well as being a broker for ZTF, it will also be one of the brokers for LSST, and is designed to be flexible enough to process a variety of astronomical data streams.

Within AMPEL, it is possible to filter alerts before they are ingested into a database, perform matches to numerous catalogues, and apply analysis methods (such as fitting to the SALT2 template) in a single pipeline. It is also possible to apply this pipeline to both alert and forced photometry from ZTF. We developed our gISNe Ia identification pipeline using the AMPEL infrastructure, specifically the astronomy analysis units from the AMPEL-HU-astro repository<sup>2</sup>. An example Python notebook that matches the structure of the pipeline is publicly available<sup>3</sup>.

Obtaining accurate lens (and host) redshifts for our candidates was the most crucial part of the study because the redshifts are necessary to estimate the absolute luminosity (and, therefore, the magnification). Several catalogues are available within AMPEL and the complete list is publicly available via the API<sup>4</sup>. The specific catalogues that we queried are listed:

1. Sloan Digital Sky Survey (SDSS) DR10 (Brescia et al. 2015);
2. NASA/IPAC Extragalactic Database (NED<sup>5</sup>), accessed through the catsHTM tool (Soumagnac & Ofek 2018);
3. Galaxy List for the Advanced Detector Era (GLADE) v2.3 (Dálya et al. 2018);
4. WISExSCOS Photometric Redshift Catalogue (WISExSCOSPZ) (Bilicki et al. 2016);
5. 2MASS Photometric Redshift catalogue (2MPZ) (Bilicki et al. 2014);
6. Legacy Survey (LS) DR8 (Duncan 2022);
7. Pan-STARRS1 Source Types and Redshifts with Machine Learning (PS1-STRM) (Beck et al. 2021).

From the LS catalogue, we obtained the galaxy colours in the  $g$ -,  $z$ -, and  $W_1$ -bands as well as the photometric redshift for

each objects. In addition to the catalogues offered by AMPEL, we cross-matched our more promising transients with the DESI spectroscopic survey. This is currently the largest spectroscopic survey operating, with the ability to observe high-redshift galaxies. Our catalogue matching to this survey is discussed in more detail in Sect. 4.2.

## 4. Candidate gISNe Ia from the ZTF archive

### 4.1. Alert pipeline

Here, we describe the functional steps of all modules of the workflow (as mentioned above, this pipeline can be reproduced using the publicly available AMPEL interface). A flowchart to summarise the entire pipeline is displayed in Fig. 3. We note that the term ‘alert’ refers to a transient event, whereas ‘object’ refers to a persistent source that is associated with the alert.

1. *Query*. Alert photometry from 1 June 2019 to 1 September 2022 was ingested based on a query with basic initial criteria. These criteria were: a point spread function (PSF) apparent magnitude of greater than 18; greater than 6 previous detections but fewer than 30; and a positive flux value.
2. *Filter*. We applied a filter that permitted SN-like alerts. The filtering criteria included a real bogus (RB) value of greater than 0.3, loose cuts on image quality (such as the full width at half maximum, elongation, and number of bad pixels), distance to known solar system objects, and an alert time history of less than 60 days. Additionally, probable stars were rejected using a match to the Pan-STARRS PS1 and the Gaia DR2 catalogues. The details of this filter are given in the DecentFilter unit of AMPEL<sup>6</sup>. The number of alerts remaining after this stage was 31930.
3. *Catalogue match*. All remaining alerts were cross-matched to the catalogues listed in Sect. 3.2 to establish whether they are associated with a galaxy. From the catalogues, we determine properties of the associated galaxy, such as the redshift and the angular separation to the alert location. If there was more than one catalogue match for a particular alert, the catalogue with the better ranking (which was based on accuracy<sup>7</sup>) was chosen. If the catalogues are ranked similarly, an average of the redshifts and distances to the galaxy were used. We note that the catalogue-matched redshift might belong to either the host or lensing galaxy. However, it will most likely belong to the lensing galaxy since this is closer and more luminous (it is unlikely the host galaxy will be sufficiently magnified). This was assumed in the following analysis.
4. *SALT2 light curve fit*. Using the Python library SNCosmo (Barbary et al. 2022)<sup>8</sup>, we performed a preliminary SALT2 fit to the alert light curves (using version 2.4, trained by Betoule et al. 2014). From this fit, we obtained a lower limit for the peak  $B$ -band absolute magnitude. This value is a lower limit because we used the catalogue-matched redshift, which we assume belongs to the potential lens.
5. *Base cuts*. We applied basic cuts intending to find transients that are most likely to be lensed. Initially, all alerts already classified as something other than a gISN by the ZTF Bright Transient Survey (BTS) were removed. We applied the following cuts on the remaining candidates:

<sup>1</sup> [github.com/AmpelProject](https://github.com/AmpelProject)

<sup>2</sup> [github.com/AmpelAstro/Ampel-HU-astro/](https://github.com/AmpelAstro/Ampel-HU-astro/)

<sup>3</sup> [github.com/AmpelAstro/Ampel-HU-astro/.../run\\_lensing\\_query.ipynb](https://github.com/AmpelAstro/Ampel-HU-astro/.../run_lensing_query.ipynb)

<sup>4</sup> [ampel.zeuthen.desy.de/api/catalogmatch/docs](https://ampel.zeuthen.desy.de/api/catalogmatch/docs)

<sup>5</sup> [ned.ipac.caltech.edu](https://ned.ipac.caltech.edu)

<sup>6</sup> [github.com/AmpelAstro/Ampel-ZTF/.../DecentFilter.py](https://github.com/AmpelAstro/Ampel-ZTF/.../DecentFilter.py)

<sup>7</sup> Details of the ranking of each catalogue are given in the T2DigestRedshifts unit of AMPEL.

<sup>8</sup> [sncosmo.readthedocs.io](https://sncosmo.readthedocs.io)

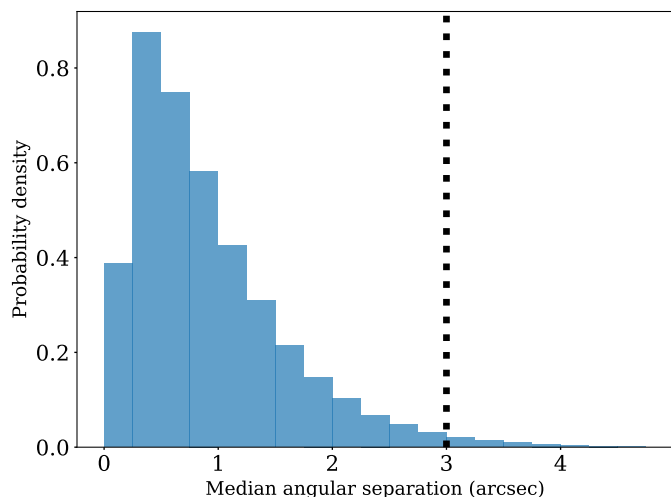


Fig. 1: A histogram that illustrates the distribution of median angular separation of simulated gISNe Ia, using data from the catalogues of Goldstein et al. (2019). The dashed black line indicates the cut that was applied in our analysis, which selects 98.4% of the distribution.

- (i) Peak  $B$ -band absolute magnitude brighter than  $-19.5$  mag. This cut selects transients brighter than normal SNe Ia. The simulations of SC24 show that the majority of gISNe Ia are in this magnitude region (regardless of whether the catalogue-matched redshift belongs to the host or the lens galaxy).
  - (ii) A redshift greater than 0.1 (also based on simulations of lens and galaxy distributions from SC24). Additionally, the probability of lensing increases at higher redshifts, due to the larger number of possible lensing galaxies, and thus a higher chance of strong lensing alignment.
  - (iii) Less than  $3''$  radius to a catalogue-matched galaxy, which ensures that the candidate is close to the lens galaxy core, where strong lensing is likely to occur. This is based on the simulated catalogues of Goldstein et al. (2019), which we utilise in Fig. 1 to show the distribution of median angular separation. From this simulation study, we calculate that 98% of the gISNe Ia have a median angular separation of less than 3 arcseconds.
  - (iv) At least five detections around the peak (within a range of 10 days before and 20 days after peak). This is required so that we can distinguish the nature of the transient from the light curve.
6. *Forced photometry.* The number of lensed candidates remaining at this stage was 7075. Next, we obtained forced photometry (FP) for these objects using the forced photometry pipeline `fpbot` developed by Reusch (2023)<sup>9</sup>, to recover data points at the lower detection limit of ZTF. This allows us to differentiate between supernovae and long-lasting transients such as active galactic nuclei (AGN) and follow the tail of said supernovae. We removed the baseline of the forced photometry data using the AMPEL unit `ZTFfpbotForcedPhotometryAlertSupplier`<sup>10</sup>. The data were truncated using the unit `T2PhaseLimit`<sup>11</sup>, which selects the portion of the light curve with a signifi-

cant supernova-like peak. The forced photometry data was utilised in the following two analysis methods of Sect. 4.2 and 4.3 to further narrow down our candidates.

We note that the following analysis is based on point source forced photometry, whereas our aim is to detect multiple point sources (e.g. two or four lensed images) that appear unresolved. For gISNe Ia with larger angular separations between the images, this can result in biased light curves.

Executing the archive search pipeline produced 7075 candidate events. This set was analysed further based on whether a DESI spectroscopic redshift was available (Sect. 4.2) or not (Sect. 4.3).

#### 4.2. Selection method 1: Spectroscopic sample with DESI cross-matching (S1)

The Dark Energy Spectroscopic Instrument (DESI; Levi et al. 2013; DESI Collaboration et al. 2016a,b, 2022, 2023, 2024a; Silber et al. 2023; Miller et al. 2023; Guy et al. 2023; Hahn et al. 2023, Bailey et al. in prep.) is a spectroscopic instrument that was designed to measure the impact of dark energy on the expansion of the Universe. The 5-year DESI survey is currently ongoing and is collecting redshifts for tens of millions of galaxies and quasars (QSOs). The DESI Y1 Key Project publications are DESI Collaboration et al. (2024b,c,d). As part of our study, collaborators working with the DESI survey contributed redshifts (including data not yet public) for galaxies and quasars that were less than  $10''$  away from our archival transients, and with redshift values greater than 0.15.

We submitted the 7075 candidates that passed the ‘base cuts’ in step 5 of the pipeline described in Sect. 4.1, for which DESI had available lens/host redshifts for 1269 of the candidates. Out of those, 519 were labelled as galaxies (and not QSOs) and within  $3''$  of the ZTF archival transient. We used the DESI redshifts where available to redo the SALT2 fits, as described in step 4 of Sect. 4.1. A total of 461 objects had a converging SALT2 fit and were utilised in the next stage of the analysis. After re-applying the base peak  $B$ -band absolute magnitude cut of  $M_B < -19.5$  mag, 257 transients remained out of the 461. From this sample, we can assert that approximately 56% of the photometrically over-luminous candidates in our sample (with a converging SALT2 fit) were also spectroscopically over-luminous (in this case, over-luminous means peak  $M_B < -19.5$  mag). This is a useful statistic for when we consider the sample with only photometric redshifts in Sect. 4.3.

Next, a stricter peak  $B$ -band absolute magnitude cut of  $M_B < -20$  mag was applied. This was done primarily to select objects that are significantly magnified, and therefore are more likely to be gISNe Ia (as opposed to belonging to over-luminous SNe Ia subclasses such as Type Ia-91T, Type Ia-CSM, or Type Ia-03fg). From the simulations of SC24, we can see that this cut removes almost all unlensed SNe Ia and approximately 20% of real gISNe Ia events. We applied this cut after obtaining forced photometry because the additional data points close to the magnitude limit should allow the SALT2 fit to better characterise the light curve shape (including the peak). In other words, we were more confident in our measurement of  $M_B$  with the forced photometry data and could apply a stricter cut.

The remaining 117 candidate light curves were inspected by eye by at least two scanners. Initially, objects were excluded if they did not look supernova-like (i.e. with long-term AGN-like variability). From this inspection, 50 candidates were selected as being possible gISNe Ia. At this point, we requested the DESI

<sup>9</sup> [github.com/simeonreusch/fpbot](https://github.com/simeonreusch/fpbot)

<sup>10</sup> [github.com/AmpelAstro/Ampel-ZTF/.../ZTFfpbotForcedPhotometryAlertSupplier.py](https://github.com/AmpelAstro/Ampel-ZTF/.../ZTFfpbotForcedPhotometryAlertSupplier.py)

<sup>11</sup> [github.com/AmpelAstro/Ampel-HU-astro/.../T2PhaseLimit.py](https://github.com/AmpelAstro/Ampel-HU-astro/.../T2PhaseLimit.py)

galaxy spectra for these candidates, to confirm that the redshifts were consistent with the spectral emission lines. The parameters for this sample of 50 are included in Table A.1.

From our spectroscopic sample of 50, we narrowed down our candidates by visual inspection once again. This time, objects were excluded if they did not look Ia-like (e.g. if they looked similar to superluminous supernovae, tidal disruption events, or AGN; refer to Sect. 5.1) or if they were previously classified on TNS. Additionally, redshifts were updated as DESI data reprocessing and re-observations occurred throughout this program, which meant that seven objects were removed from the sample. Consequently, we had 27 final candidates from the spectroscopic sample, which are discussed in Sect. 4.4 and shown in Table 3.

#### 4.3. Selection method 2: Photometric sample from selection with additional cuts (S2)

The majority of the objects that passed the base cuts described in Sect. 4.1 did not have a spectroscopic redshift from DESI. It was not possible to manually inspect these remaining objects, so we applied further cuts motivated by the simulations of SC24 and observational data. For example, Fig. 2, illustrates the LS  $g - z$  vs.  $g - W_1$  lens galaxy colours for the sample of candidates remaining after the base cuts within the redshift bin  $0.2 < z < 0.3$ . By comparing to catalogues of known lens galaxies<sup>12</sup> and QSOs (from the WISE catalogue of AGN; Assef et al. 2018), it is evident that a large fraction of the candidates' associated galaxies do not have the expected colours of a lensing galaxy.

By implementing stricter cuts, we aimed to increase the likelihood that a transient was truly a lensed supernova, even though photometric redshifts are less reliable. We required that the transient more closely resembled the expected features of a gISN Ia. These characteristics include the light curve colour evolution, the lens galaxy colours, and the SALT2 fit parameters. We note that the additional cuts were applied to all remaining candidates at the end of Sect. 4.1, not just the objects without a DESI galaxy match in Sect. 4.2. The additional cuts were as follows:

1. *SALT2 light curve refit.* First, we refitted the light curves with the SALT2 template, to recalculate the peak absolute magnitude values from the new forced photometry data. If a SALT2 fit could not converge, or the new peak absolute magnitude was dimmer than  $-20$  mag, the candidate was removed from the sample. The justification for this stricter absolute magnitude cut is the same as in Sect. 4.2.
2. *Additional cuts.* The remaining candidates were selected based on a set of further cuts:
  - (i) *Light curve colour cuts.* A selection of  $g - r$ ,  $g - i$ , and  $r - i$  colour cuts at light curve phases of  $t_0 - 7$ ,  $t_0$ , and  $t_0 + 7$  days (where  $t_0$  is the time at peak  $B$  magnitude) were determined based on simulations from SC24. The values for these cuts are summarised in Table 1. The motivation for these cuts is that they differentiate normal Type Ia supernovae from lensed ones, given that the latter are usually significantly redder (when observed at the same peak apparent magnitude). In SC24, the simulations show that this is the colour space where we expect to find 90% lensed and 10% unlensed SNe Ia. Candidates were labelled as passing this cut if they passed at least one of the colour cuts at a certain epoch. The leniency

<sup>12</sup> L. A. Moustakas, J. Brownstein et al., priv. comm. The Master Lens Database of confirmed and probable lenses from various sources. <http://admin.masterlens.org>

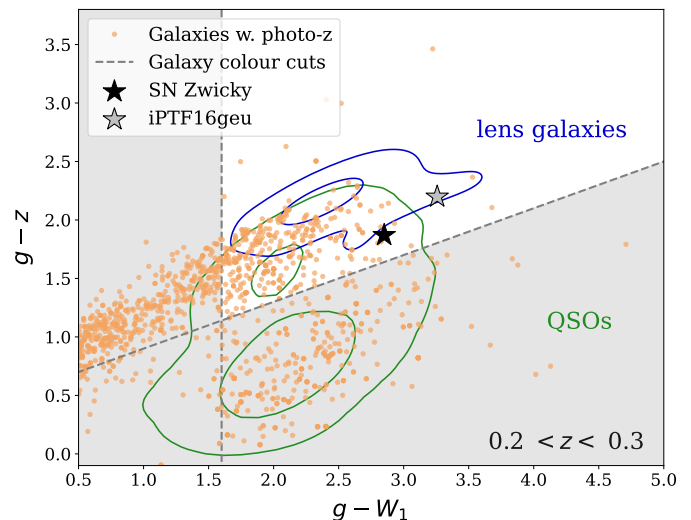


Fig. 2: A plot of the LS  $g - z$  vs.  $g - W_1$  galaxy colours for the candidates remaining after the base cuts (orange), compared to contours from confirmed and candidate lens galaxies (blue), and QSOs detected by WISE (green). The data was acquired by cross-matching the AGN and lens catalogues with LS (Duncan 2022). The dashed lines indicate the colour cuts which were devised to select likely elliptical and lens galaxies, shown in Table 2. A single redshift bin of  $0.2 < z < 0.3$  is shown for clarity. The two star markers show the lens galaxy colours for iPTF16geu (grey) and SN Zwicky (black), which had lens redshifts of 0.216 and 0.226, respectively. For SN Zwicky, the  $g - z$  vs.  $g - W_1$  colours from Pan-STARRS are shown instead, because the lens galaxy was not present in the LS catalogue).

of this cut is due to some light curves missing bands – usually the  $i$ -band – and/or certain epochs. Additionally, we used light curve information from a window of  $\pm 3$  days around the phases of  $t_0 - 7$ ,  $t_0$ , and  $t_0 + 7$  days, so that we did not penalise objects that were observed with a cadence of two or three days.

Table 1: Light curve colour cuts for the  $g$ -,  $r$ - and  $i$ -bands applied at a phase of  $t_0 - 7$ ,  $t_0$ , and  $t_0 + 7$  days.

Phase (days)	Light curve colour cut (>)		
	$g - r$	$g - i$	$r - i$
$t_0 - 7$	-0.08	-0.08	-0.34
$t_0$	0.12	0.06	-0.28
$t_0 + 7$	0.33	0.33	-0.23

**Notes.** The values are based on simulations from SC24.

- (ii) *Galaxy colour cuts.* Using galaxy colours from LS, we implemented colour cuts that aimed to exclude AGN and blue star-forming galaxies whilst retaining lens-like galaxies. For this cut, we assumed that the catalogue-matched galaxy is the lens or a blend of the lens and the SN host galaxy (the blended systems, similar to iPTF16geu, will be more in the upper right corner, and so will also be preserved with the cuts). The values are chosen from the empirical observations in Fig. 2 and are given in Table 2. Additionally, a minimum galaxy brightness of greater than 21.07 in the LS  $z$ -band (corrected for Milky Way extinction) was required. This was based on simulations of lens galaxies from Wojtak et al.

(2019) and Arendse et al. (2023) with K-corrections from Lenspop (Collett 2015)<sup>13</sup>. The simulations show that we expect 90% of lens galaxies to be brighter than this magnitude limit.

Table 2: Table of galaxy colour cuts for the LS  $g$ -,  $z$ - and  $W_1$ -bands in different redshift bins.

Redshift bin	Galaxy colour cuts
$0.1 < z < 0.2$	$(g - z) > 0.2 + 0.4 \times (g - W_1)$ $(g - W_1) > 1.0$
$0.2 < z < 0.3$	$(g - z) > 0.5 + 0.4 \times (g - W_1)$ $(g - W_1) > 1.6$
$0.3 < z < 0.4$	$(g - z) > 0.9 + 0.3 \times (g - W_1)$ $(g - W_1) > 2.2$
$0.4 < z < 0.5$	$(g - z) > 0.45 + 0.4 \times (g - W_1)$ $(g - W_1) > 2.3$
$0.5 < z < 0.6$	$(g - z) > 0.3 + 0.4 \times (g - W_1)$ $(g - W_1) > 2.5$
$z > 0.6$	$(g - z) > -0.1 + 0.5 \times (g - W_1)$ $(g - W_1) > 1.0$

**Notes.** The cuts are derived from the observations in Fig. 2, to exclude AGN and blue star-forming galaxies but retain lens-like galaxies.

- (iii) *SALT2  $c$  parameter.* Based on the simulated distributions shown in SC24, we predict that 90% of gISNe Ia light curves have a SALT2 colour parameter,  $c$ , of greater than 0 (which is synonymous with being redder). Thus, a cut of  $c > 0$  was applied to the sample.
- (iv) *SALT2  $x_1$  parameter.* As discussed in Sect. 2, we expect that gISNe Ia with narrower light curves will have a greater total magnification (and conversely, wider light curves will have a smaller total magnification). This means that there are likely two populations of gISNe Ia: less magnified objects with larger  $x_1$  values that may have poor SALT2 fits, and more magnified objects with smaller  $x_1$  values that more closely resemble normal SNe Ia. The transients observed with greater magnification will have a better line-of-sight alignment with the core of the lensing galaxy, meaning that the distance to the catalogue-matched galaxy should be less (the actual value depends on the Einstein radius of the lensing system, but for typical compact systems we would expect a separation of  $\theta < 1''$ ). This information suggests that we could study the two populations separately so that we could remove contamination by normal SNe Ia more easily. We implemented this hypothesis as follows:
- To select the highly magnified gISNe Ia with smaller time delays, we applied a SALT2 stretch cut of  $-3 < x_1 < 3$ , which would select the objects that look like normal SNe Ia. Additionally, we required that the object was less than  $1''$  away from the catalogue counterpart, to increase the likelihood that the object was a highly magnified gISN Ia.
  - To select the less magnified gISNe Ia, we applied a SALT2 stretch cut of  $3 < x_1 < 20$ , which would exclude the normal SNe Ia. This cut is motivated by the distribution of  $x_1$  parameters for simulated lensed and unlensed SNe Ia in SC24.

We note that a small angular separation to the lensing galaxy was used as a proxy for magnification, instead of the peak ab-

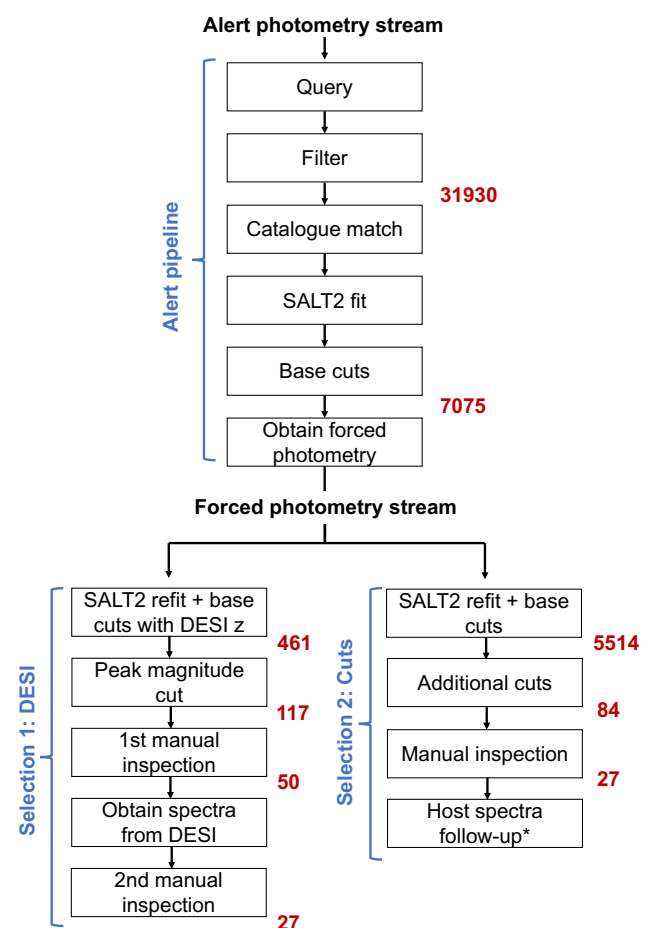


Fig. 3: A flowchart to illustrate the stages of the method, as described in Sect. 4. The red numbers to the bottom-right of the boxes indicate the number of transients that remained after that stage of the analysis. The asterisk represents a stage that has not been completed during our study and is left for future work.

solute magnitude, to minimise the impact of inaccurate photometric redshifts.

3. The candidates were inspected by eye by at least two scanners. Objects were excluded if they did not look Ia-like (i.e. if they looked similar to other transients, such as the contaminants discussed in Sect. 5.1), if they were classified as something else, or if the data was too limited or noisy to determine what they were.

After this manual inspection stage, 27 photometric candidates were remaining. Seven of the candidates also had a DESI cross-match and were identified in the spectroscopic sample from Sect. 4.2. The 27 photometric candidates are discussed in detail in Sect. 4.4 and shown in Table 4.

A discussion of the accuracy of the various photometric catalogues utilised in this study is beyond the scope of this paper. However, from our analysis in Sect. 4.2, we can assume that at least half of the photometrically over-luminous candidates identified in this selection method would also be spectroscopically over-luminous, if a spectrum for the lens/host was obtained.

The methodology described in Sect. 4 is summarised as a flowchart in Fig. 3, which includes the number of transients that remained after each stage in the analysis (indicated in red).

<sup>13</sup> [github.com/tcollett/LensPop](https://github.com/tcollett/LensPop)

## 4.4. Summary of candidates

Table 3 summarises the 27 candidates from S1 described in Sect. 4.2, with spectroscopic redshifts and angular separations from a catalogue match with DESI. This selection of spectroscopically over-luminous candidates is interesting since we expect that the majority of the events are bright enough to be gISNe Ia. However, if they do not pass the cuts specified in Sect. 4.3, it is more likely that they are superluminous supernova candidates. Despite this, we cannot exclude the possibility that some of them are gISNe Ia (or other lensed transients) and the reason(s) that they did not pass the cuts are:

1. The fit to the SALT2 template fails to model the light curve well enough, which may be the case if the lensed object is not a typical SN Ia or it is a Type II supernova. This could mean that it does not pass the  $x_1$ ,  $c$ , and light curve colour cuts, or that a SALT2 fit does not converge at all.
2. The catalogue-matched galaxy information is not present in the LS catalogue, the LS catalogue galaxy is dimmer, or the colours are different than what we would expect from a lens galaxy. This would mean that it does not pass the galaxy cuts.

Table 3: Spectroscopic sample

ZTF ID	DESI $z$	Ang. sep. (")	Peak $M_B$
ZTF19aarzfoz	0.1765	0.87	-20.00
ZTF19aavrvoe	0.2894	0.07	-20.87
ZTF19abdbshk	0.2832	2.23	-21.15
ZTF19abpjicm	0.2383	0.92	-20.00
ZTF20aarvtor	0.3192	1.07	-20.56
ZTF20aatpwrh	0.3357	1.03	-20.92
ZTF20aawabry	0.2930	0.94	-20.85
ZTF20aawlfwk	0.3138	0.17	-20.64
ZTF20abatzio	0.2872	0.63	-20.57
ZTF20abfhluf	0.2198	0.96	-20.59
ZTF20abjyrxf	0.2199	0.76	-20.47
ZTF20acirhoc	1.3710	1.34	-26.58
ZTF20aclwssg	0.3309	0.31	-21.60
ZTF20acmvzuo	0.1762	1.14	-20.21
ZTF20acxtayx	0.2041	0.84	-20.69
ZTF21aablrfe	0.3072	2.35	-20.34
ZTF21aacsoko	0.2287	0.12	-20.61
ZTF21aapreug	0.2222	0.43	-20.93
ZTF21abcwuhh	0.3334	1.57	-20.17
ZTF21abfvefa	0.3288	1.81	-20.93
ZTF21abwppte	0.2163	1.12	-20.42
ZTF22aabifrp	0.1886	2.85	-20.94
ZTF22aadeqlh	0.3225	2.71	-21.61
ZTF22aahmovu	0.2429	0.65	-20.34
ZTF22aaqkvvm	0.3775	2.81	-21.35
ZTF22aatstmd	0.3120	2.90	-21.09
ZTF22aaiuhjc	0.2690	0.28	-20.38

**Notes.** The error on the DESI redshift values is 0.0001. The full table including the right ascension (RA), declination, and SALT2 fit parameters is Table A.1 in the Appendix.

To eliminate these possibilities, careful inspection of each of the candidates is necessary. To increase the likelihood that a candidate is a gISN Ia, we could fit the light curves to a combined SALT2 model with multiple images, and check that the resulting fit parameters are reasonable compared to the results from simulation studies.

Table 4: Photometric sample

ZTF ID	Phot. $z$	Ang. sep. (")	Peak $M_B$
ZTF19abamkfs	0.29	0.40	-21.22
ZTF19abctwkl	0.22	0.04	-20.07
ZTF19abdkdze	0.18	2.39	-20.17
ZTF19abheyzp	0.23	0.34	-20.80
ZTF19abpfedt	0.16	0.97	-20.06
ZTF19abpjicm	0.24	0.87	-20.06
ZTF19adbmdsa	0.18	0.53	-20.11
ZTF20aahgirj	0.17	0.75	-20.13
ZTF20aaiqpgv	0.29	0.69	-20.12
ZTF20abjyrxf	0.19	0.78	-20.15
ZTF20ablmtxz	0.26	0.18	-20.26
ZTF20aceekkd	0.16	0.69	-20.35
ZTF20achutix	0.25	2.20	-20.55
ZTF20acotfan	0.23	0.25	-20.21
ZTF21aablrfe	0.31	2.35	-20.35
ZTF21aaxvxbu	0.24	0.51	-20.61
ZTF21abawmyd	0.26	0.86	-20.31
ZTF21abcwuhh	0.34	1.55	-20.21
ZTF21acdypeu	0.19	0.67	-20.10
ZTF21acmqvww	0.25	0.97	-20.06
ZTF22aabfojs	0.19	0.21	-20.72
ZTF22aabifrp	0.25	0.14	-21.45
ZTF22aadeqlh	0.27	2.65	-21.11
ZTF22aahmovu	0.22	0.58	-20.05
ZTF22aamltry	0.16	1.02	-20.21
ZTF22aaoncel	0.19	0.19	-20.39
ZTF22abakgnp	0.25	0.62	-20.25

**Notes.** The full table including the right ascension (RA), declination, and SALT2 fit parameters is Table A.1 in the Appendix.

Table 4 summarises the 27 candidates from S2 described in Sect. 4.3, with the photometric redshifts and angular separations from catalogue matches within AMPEL. Unfortunately, without reliable host or lens redshifts, it is hard to assign a confidence level to the claim that a candidate is truly a lensed supernova, because of uncertainty in the absolute brightness. Therefore, the photometric sample in Table 4 will need to be targeted in future spectroscopic follow-up missions to get the lens and host redshifts before we can make any conclusions about them being gISNe Ia. At the time of publication, this was not yet possible, but it is something that we aim to do in future work.

## 5. Sample properties

## 5.1. Sources of contamination

Five main sources of contamination may have passed the cuts in our pipeline: AGN, tidal disruption events (TDEs), superluminous supernovae (SLSNe), lensed core-collapse SNe, and unlensed SNe Ia (either due to their peculiar over-luminosity or an incorrect photometric redshift).

Firstly, AGN are luminous enough to look similar to lensed events and constitute a large fraction of the 7075 transients that pass the base cuts with alert photometry. However, they were likely removed by the cuts applied in Sects. 4.2 and 4.3 after we obtained the forced photometry (because the FP should contain any long-term variations that were slightly below the detection threshold for the alert photometry). Even if there were AGN that passed these additional cuts, the long-term variability in the light curves would be clear enough to remove during



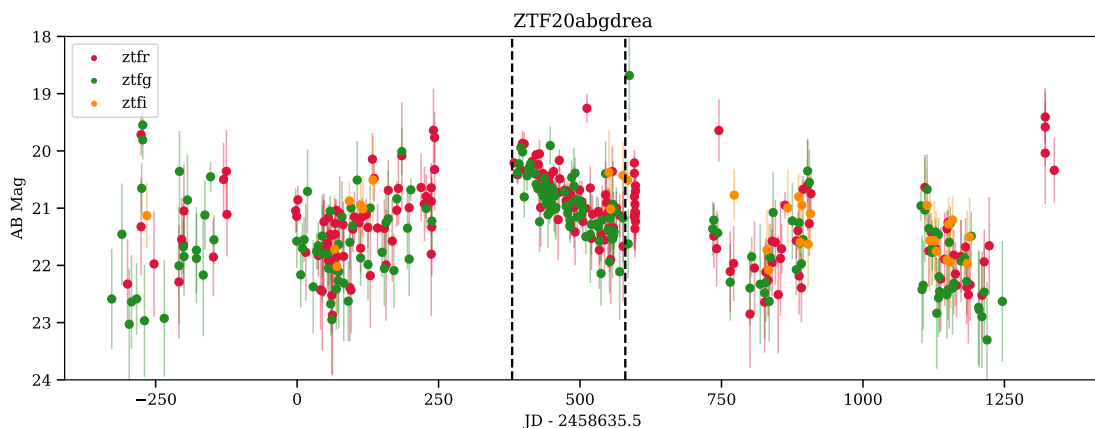


Fig. 4: The light curve of ZTF20abgdrea, a candidate that passed S1 and S2, but was removed during visual inspection due to the long-term variability that suggests it is a likely AGN/QSO. The black dotted lines indicate the section of the light curve that was selected by the pipeline for the SALT2 fit. The baseline was not removed from this forced photometry, to more clearly illustrate the variability.

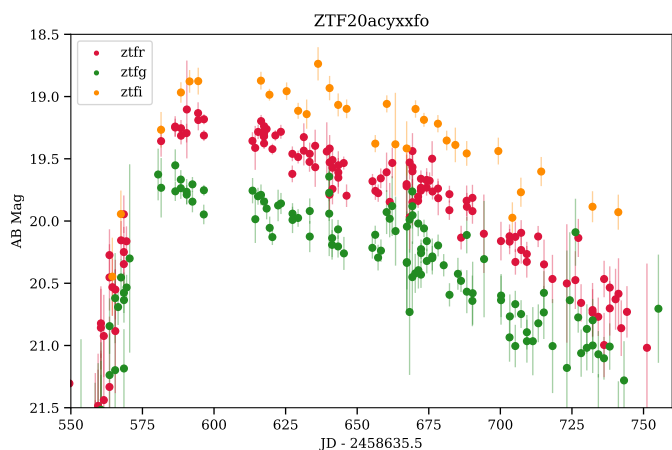


Fig. 5: The light curve of ZTF20acyxxfo, a candidate that passed S1 and S2, but was removed during visual inspection because it was identified as a likely TDE due to the approximate power-law decline.

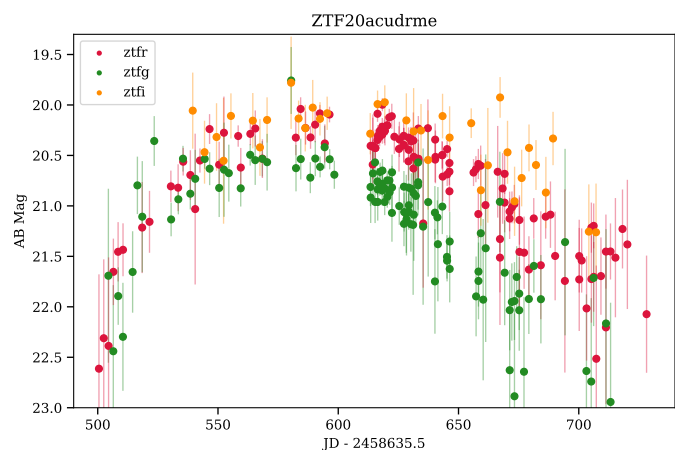


Fig. 6: The light curve of ZTF20acudrme, a candidate that passed S1, but was removed during visual inspection because the long duration indicates it is a likely SLSN.

the visual inspection stages. An example of this in our study is ZTF20abgdrea, shown in Fig. 4. This object was present in both selection methods but was filtered out during the visual inspection stage. The black dotted lines indicate the section of the light curve that was selected by the pipeline for the SALT2 fit, which explains why it passed our stringent cuts from selection method 2 (S2). Additionally, ZTF20abgdrea is  $0.7''$  away from a candidate lens system in the SuGOHI VI catalogue (Sonnenfeld et al. 2020), which means that it could also be a lensed AGN/QSO. However, the DESI spectrum shows no evidence of AGN activity, so this is not possible to confirm without further study of the lens system.

Secondly, TDEs reside close to galaxy cores and can also be very luminous, so they satisfy most of our criteria. However, they are quite rare events (although not as rare as gISNe Ia) and their light curves have distinct features, such as an approximate power-law decline, and are sometimes accompanied by a dust echo (for example, detected in the WISE infrared bands) (Reusch et al. 2022). This distinctive light curve shape allowed us to iden-

tify and remove likely TDEs from our sample. An example of this is ZTF20acyxxfo, shown in Fig. 5. This object (with a DESI redshift of  $z = 0.2$  which implies a peak  $M_B < -20$  mag) was present in both selection methods but was filtered out during the visual inspection stage, as it has a good fit to a TDE template light curve (Reusch et al., in prep.).

Thirdly, SLSNe are a large contaminant because they are very luminous (with a peak absolute magnitude of approximately  $-21$ ) and some of their light curves closely resemble the light curves of gISNe Ia with longer time delays. However, we can exclude some SLSNe with longer durations that would not be feasible for gISNe Ia (i.e. a rest-frame duration of greater than 100 days). Additionally, the galaxy brightness cut that we describe in Sect. 4.3 should exclude the hosts of hydrogen-poor superluminous supernovae (SLSNe-I), which are typically bluer and fainter (Lunnan et al. 2014; Leloudas et al. 2015; Schulze et al. 2018). To fully exclude SLSNe as contaminants, careful examination of each candidate and all the data available is necessary – we perform this examination in Sect. 6 for our most likely candidates. An example of a possible SLSN that we re-

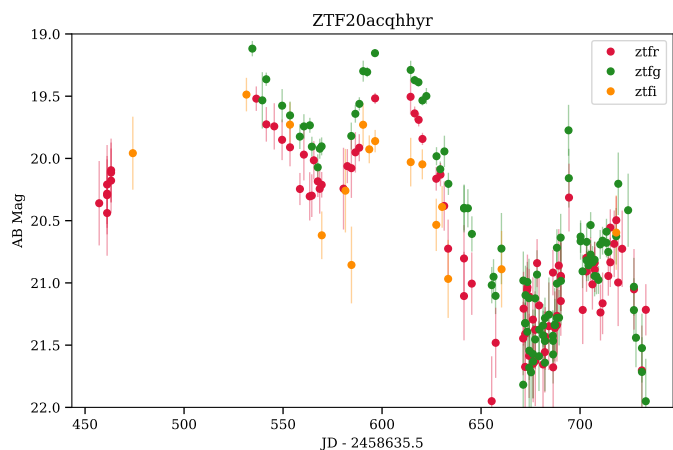


Fig. 7: The light curve of ZTF20acqhhyr, a candidate that passed S1, but was removed during visual inspection because of the presence of multiple bumps in the light curve of not-equal width, which suggests that CSM interaction is causing the high luminosity.

moved during the visual inspection stage of S2, ZTF20acudrme, is displayed in Fig. 6. This object had a photometric redshift of  $z = 0.25$ , which allowed us to estimate a peak  $M_B < -20$  mag. However, the long duration and large separation from its galaxy counterpart (at  $2''$ ) suggest that ZTF20acudrme is a SLSN candidate.

Additionally, some lensed core-collapse supernovae may be present in this sample. Typically, core-collapse SNe have a peak  $B$  absolute magnitude of approximately  $-17$  (Perley et al. 2020), which means that they would have to be extremely magnified to pass our final peak cut of  $M < -20$  mag. Additionally, the simulations of SC24 showed that applying a  $c > 0$  cut should remove almost all lensed core-collapse SNe. This significantly reduces the probability of their detection by our algorithm, although their presence is not ruled out. If we did find something magnified, but looked more similar to a core-collapse SN than a Type Ia SN, we would not exclude it from our analysis (as this would also be an interesting discovery). However, none of the candidates in our sample have the obvious characteristics of a lensed core-collapse supernova.

Transients that interact with the circumstellar material (CSM) are possible contaminants. Supernova classes like Type Ia-CSM and Type IIn can be more luminous than normal SNe Ia due to the supernova ejecta interacting with material that surrounds the progenitor, causing an increase in the brightness we observe (Sharma et al. 2023). However, typically the light curve will display signatures of CSM interaction, such as multiple bumps or plateauing phases. Fig. 7 illustrates an example candidate that was removed during the visual inspection of S1, due to the multiple peaks of varying widths, which could not be caused by a multiply imaged SN.

Other peculiar sub-classes of SNe Ia can be over-luminous, such as 03fg-like (or super-Chandrasekhar) and 91T-like SNe Ia. SNe Ia-03fg are believed to be the result of white dwarf progenitors that exceed the Chandrasekhar limit before they explode (Howell et al. 2006). These objects can surpass a peak  $M_B$  of  $-20$  mag, however, they are typically less red than what we expect from gISNe Ia so it is unlikely they would pass our light curve colour cuts in Sect. 4.3. Similarly, SNe Ia-91T are believed to arise from non-typical progenitor systems that cause the SN explosion to be more luminous. Yet, SNe Ia-91T are typically

0.2 mag brighter than normal SNe Ia (Yang et al. 2022), so it is unlikely that they would pass our peak magnitude cut.

Finally, we note that some objects with erroneous photometric redshifts will be present in the photometric sample in Table 4. These are likely to be normal SNe Ia at redshifts of  $z \sim 0.1$ .

## 5.2. Comparison with the Bright Transient Survey (BTS)

BTS is a spectroscopic supernova survey within ZTF that aims to acquire spectra of all transients brighter than 18.5 magnitudes (excluding galactic sources, AGN, or moving objects), using the Spectral Energy Distribution Machine (SEDM) that operates on the Palomar 60-inch telescope (Blagorodnova et al. 2018). The survey aims to create the largest unbiased, brightness-limited sample of supernovae. Additionally, they target objects brighter than 19 magnitudes when the spectroscopic resources are available. The first spectrum of SN Zwicky was obtained as a result of BTS scanners submitting it to the SEDM for spectroscopic classification (Goobar et al. 2023).

To quantify the amount of contamination from unlensed supernova-like sources in this study, a comparison to the BTS was performed. We obtained forced photometry for 4127 transients in the BTS catalogue<sup>14</sup> with a redshift (including the classes SLSN, SN Ia, SN Ib/c, TDE, and their subclasses), and processed the data as described in step 6 of Sect. 4.1. A SALT2 template fit was performed, as described in step 4 of the aforementioned section, using the redshift from the BTS catalogue. Figure 8 shows a histogram with the derived peak  $M_B$  from the SALT2 fits for all the objects in the sample. Finally, we applied the base cuts as described in step 5 of the pipeline ( $M_B < -19.5$  mag,  $z > 0.1$ , less than  $3''$  distance from a catalogue-matched galaxy, at least 5 detections around the peak). The objects that remained after these cuts are shown by the black histogram line in Fig. 8.

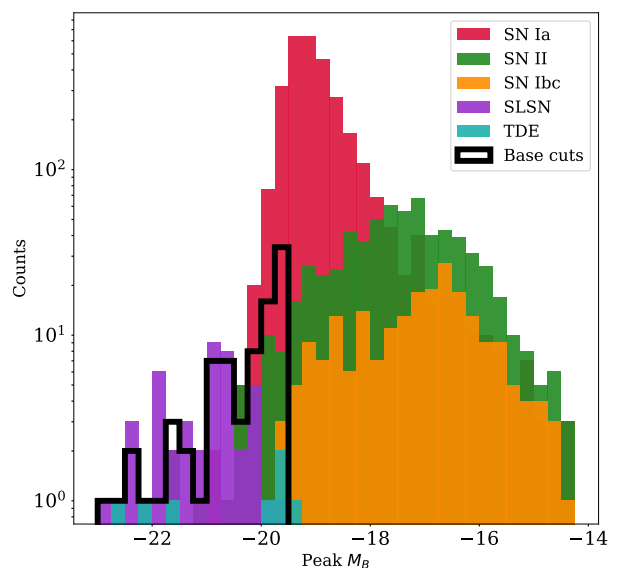


Fig. 8: A histogram that illustrates the peak B absolute magnitude distribution for the 5 main classes of transients (Type Ia, Type II, Type Ib/c, SLSNe, and TDEs) recorded by the BTS. The black outline illustrates the objects remaining after applying the base cuts from our pipeline.

<sup>14</sup> Publicly available here: [sites.astro.caltech.edu/ztf/bts/explorer.php](https://sites.astro.caltech.edu/ztf/bts/explorer.php)

In the sample remaining after base cuts, we retained 43% of the original SLSNe, 29% of the TDEs, 2% of the SNe II (of which the majority were Type II<sub>n</sub>), 2% of the SNe Ia, and less than 1% of the SNe Ib/c. After applying the stricter peak absolute magnitude and redshift cuts described in Sects. 4.2 and 4.3, the only contamination in the sample is due to SLSNe (24% remaining), TDEs (14% remaining), and a small contribution from SNe II (less than 1% remaining). After applying all the cuts described in Sect. 4.3, only one object remains (ZTF21aahfjrr, classified as a Type II<sub>n</sub>, but likely a SLSN-II<sub>n</sub>). This study illustrates that we should expect non-negligible contamination from SLSNe and TDEs from the selection method of Sect. 4.2, but very little contamination from the method of Sect. 4.3.

### 5.3. Comparison with known gISNe Ia

It is valuable to compare the statistics of our candidates to the gISNe Ia already observed by ZTF and iPTF. Figure 9 shows the distribution of the peak *B*-band absolute magnitude vs. the redshift for the candidates in the sample, assuming that the object is at the lens redshift. This peak absolute magnitude would be a lower limit on the true peak if the object is truly lensed. The blue contour displays the transients that passed the base cuts described in Sect. 4.1 and the data points illustrate the candidates passing the two selection methods (S1 and S2) described in Sects. 4.2 and 4.3, respectively. The corresponding values for SN Zwicky and iPTF16geu are also displayed. From Fig. 9, it is apparent that SN Zwicky and iPTF16geu match the brightest magnification tail. This implies that, if our candidates are truly gISNe Ia, they would belong to a less magnified population. Excluding a single high redshift candidate from the S1 sample (ZTF20acirhoc,  $z = 1.4$ ), the majority of the candidates are found to have lens galaxies within the range  $0.2 < z < 0.4$ .

Figure 10 shows the distributions for peak *B*-band apparent magnitude ( $m_B$ ), peak *B*-band absolute magnitude ( $M_B$ ), lens redshift ( $z$ ), SALT2  $x_1$ , SALT2  $c$ , and angular separation values for the transients that passed each stage of the cuts (the base cuts, S1 and S2). For comparison, the dotted line with a star marker indicates the corresponding values for SN Zwicky for each distribution parameter, using the values given in Goobar et al. (2023) (with the caveat that the SN Zwicky parameters were fitted using a SALT2 time-delay model with four separate images, whereas our pipeline is only fitting for one resulting SALT2 light curve).

Additionally, we applied our pipeline to the alert photometry for SN Zwicky and found that it passed all of the base cuts as well as all of the additional cuts described in Sect. 4.3, except for the galaxy colour cuts (as they rely on Legacy Survey data, which is not available for this area of sky). However, as shown in Fig. 2, a catalogue counterpart for SN Zwicky observed by Pan-STARRS would have passed our galaxy colour cuts.

## 6. Gold sample of gISN Ia candidates

There is a subsample of candidates that pass all the cuts described in Sect. 4.3 and also have a cross-match with a galaxy counterpart observed by DESI. Table 5 summarises the candidates that were found by both selection methods. Hereafter we shall refer to this sample of candidates as the ‘gold sample’. The light curves for the seven candidates in the gold sample are displayed in Fig. 11, which includes their DESI galaxy redshift and peak absolute magnitude (assuming the object is located at the catalogue redshift). Additionally, the Legacy Survey (LS) field cutouts for the seven candidates are shown in Fig. 12, where the location of the ZTF transient is indicated by a green circle. This

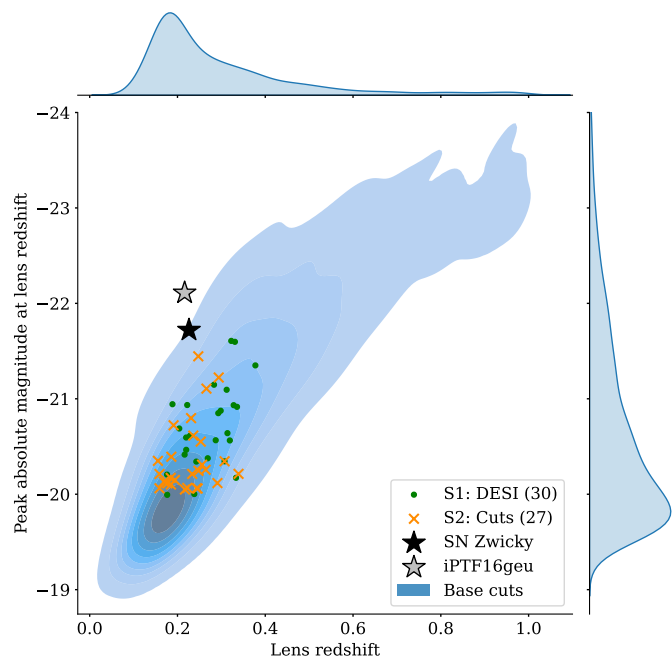


Fig. 9: The distribution of the peak *B*-band absolute magnitude at the lens redshift vs. the lens redshift for the transients that passed the base cuts described in Sect. 4.1 (blue contours), the candidates passing the two selection methods described in Sects. 4.2 and 4.3 (green and orange crosses, respectively), and for the already discovered gISNe Ia SN Zwicky and iPTF16geu (black and grey stars, respectively). The upper limit of the *x*-axis has been adjusted for clarity, omitting one higher redshift objects from S1 (ZTF20acirhoc).

sample represents our most likely gISN Ia candidates because we are confident that they are more luminous than normal SNe Ia and they have the expected light curve and lens galaxy characteristics of gISNe Ia.

Table 5: Gold sample

ZTF ID	Phot. $z$	DESI $z$	Peak $M_B$ (DESI)
ZTF19abpjicm	0.24	0.24	-20.00
ZTF20abjyrxf	0.19	0.22	-20.47
ZTF21aablrfc	0.31	0.31	-20.34
ZTF21abcwuhh	0.34	0.33	-20.17
ZTF22aabifrp	0.25	0.19	-20.94
ZTF22aadeqlh	0.27	0.32	-21.61
ZTF22aahmovu	0.22	0.24	-20.34

**Notes.** The full table including the right ascension (RA), declination, and SALT2 fit parameters is Table A.1 in the Appendix.

In the following subsections, we examined the seven gold sample candidates further by fitting to a simple two-image SN Ia model (Sect. 6.1), calculating the rise, decline, and duration of the light curves (Sect. 6.2), and by obtaining the galaxy photometry (Sect. 6.3). Each object is also discussed in depth, starting with the the most likely candidates (Sect. 6.4).

### 6.1. Two-image combined SALT2 fit

We fitted the light curves of the gold sample to a combined SALT2 model with two images. While simulations from Gold-

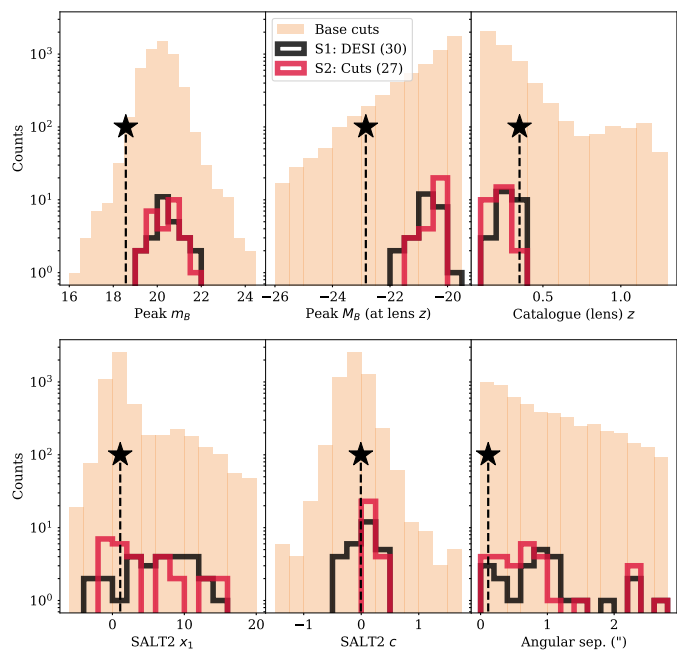


Fig. 10: A set of histograms that display the distributions for peak  $m_B$ , peak  $M_B$ , lens  $z$ , SALT2  $x_1$ , SALT2  $c$ , and angular separation values for the transients that passed the base cuts described in Sect. 4.1 (orange bars), and the candidates passing the two selection methods described in Sects. 4.2 and 4.3 (black and red solid lines, respectively). The dotted line with a star marker indicates the corresponding values for SN Zwicky for each distribution parameter.

stein et al. (2019) predict that most events detected by ZTF would have four images (at a percentage of 62%, vs. 22% for two images), constraining the parameters for four images simultaneously is challenging without additional information about the system (e.g. the flux ratios of the images to constrain each magnification) and also not possible with the limited number of detections we have for some candidates. By including a second component to the SALT2 light curve, we can show that the transient differs from a typical unlensed SN, which strengthens the argument that the object is multiply imaged. The combined model, in flux space, is given as

$$f_{\text{model}}(t) = F_1 \times f_{\text{SALT2}}(t) + F_2 \times f_{\text{SALT2}}(t - \Delta t), \quad (1)$$

where  $F_1$ ,  $F_2$  are the relative image magnifications,  $\Delta t$  is the second image time delay (in the observer-frame),  $t$  is the phase of the light curve, and  $f_{\text{SALT2}}$  is the flux model for a single SALT2 template. The SALT2 model is also dependent on the following parameters: the time of the light curve peak ( $t_0$ ), the amplitude ( $x_0$ ), colour ( $c$ ), and stretch ( $x_1$ ) of the light curve, and the redshift of the transient ( $z$ ). We note that these image magnifications are relative, and not absolute values. If we assume that the lenses can be modelled as a singular isothermal sphere/halo (SIS), then the absolute total image magnification (which is the sum of the individual image magnifications) for the two-image system is given by

$$\mu_{\text{tot}} = \frac{2(r+1)}{r-1}, \quad (2)$$

where we define the flux ratio as  $r = F_1/F_2$ .<sup>15</sup>

We allowed the redshift parameter to vary between a lower limit of the DESI  $z$ , and two times this value. This is because we expect the DESI  $z$  to belong to the lens, and the actual supernova will belong to a more distant background galaxy. To prevent a degeneracy with the image magnifications, the intrinsic amplitude of the SNe Ia light curve ( $x_0$ ) is fixed to be an arbitrary value. We iterated through different values of the stretch parameter and allowed the time delay for the second image to vary between zero and 60 days (this value is motivated by the simulations of SC24 and Goldstein et al. 2019, and also implied by the absence of a distinct secondary peak).

Table 6: Two-image combined SALT2 model parameters for the gold sample

Parameter	ZTF19abpjcm	ZTF20abjyrxf	ZTF22aahmovu
$z$	$0.44 \pm 0.05$	$0.24 \pm 0.02$	$0.35 \pm 0.01$
$t_0$ (MJD)	$58710 \pm 2$	$59069 \pm 1$	$59692 \pm 1$
$x_0$	$(2 \pm 1) \times 10^{-4}$	$(6 \pm 1) \times 10^{-4}$	$(2 \pm 1) \times 10^{-4}$
$x_1$	$0.13 \pm 0.97$	$2.00 \pm 0.05$	$2.00 \pm 0.06$
$c$	$-0.23 \pm 0.05$	$-0.11 \pm 0.04$	$0.00 \pm 0.02$
$\Delta t$ (days)	$22 \pm 3$	$27 \pm 1$	$34 \pm 1$
$F_1$	$0.46 \pm 0.16$	$0.28 \pm 0.06$	$0.72 \pm 0.08$
$F_2$	$0.13 \pm 0.06$	$0.23 \pm 0.05$	$0.26 \pm 0.03$
$\mu_{\text{tot}}$	$3.6 \pm 1.3$	$20.4 \pm 6.2$	$4.3 \pm 0.6$
$\chi_r^2$	0.86	2.53	1.38

Out of the seven candidates in the gold sample, only three of them converged to reasonable two-image combined SALT2 fits: ZTF19abpjcm, ZTF20abjyrxf, and ZTF22aahmovu. Figure 13 illustrates the best fit two-image model for each candidate and Table 6 displays the fit parameters (as well as the derived parameters  $\mu_{\text{tot}}$ ,  $\mu_1$ , and  $\mu_2$ ) for each model. The best fit time delays are larger than what we observed for SN Zwicky (where the time delays for all the images were less than a day) but are not unexpected, according to the simulations of SC24. They find that the median maximum time delay for gISNe Ia with a peak apparent magnitude of  $m > 19$  is 8.9 days in the rest-frame (which would correspond to 12.5 days in the observer-frame, assuming a gISN at  $z = 0.4$ ). Additionally, they predict that approximately 20% of gISNe Ia in this magnitude regime would have maximum time delays of greater than 25 days in the rest-frame.

The remaining four objects in the gold sample have poor combined two-image SALT2 fits because they are too wide to only display a single peak (ZTF21aablrfe, ZTF22aabifrp, and ZTF22aadeqlh) or they are too noisy to provide a convincing fit (ZTF21abcwuhh). The two-image fits for the wide objects produced larger time delays, for which we would have expected two distinct light curve peaks. However, this is not evident from any of the light curves. We note that a model with three or four images could explain the wider light curves and the absence of bumps, but this is not something that we explicitly modelled (due to the difficulty in constraining the extra model parameters).

Additionally, we calculated the expected image separation ( $\Delta\theta$ ) from our best-fit two-image SALT2 parameters. Once again assuming the lens to be an SIS, we have the following equation

<sup>15</sup> For completeness, the individual image magnifications are given as

$$\mu_1 = \frac{2r}{r-1}, \quad \mu_2 = \frac{2}{r-1}. \quad (3)$$

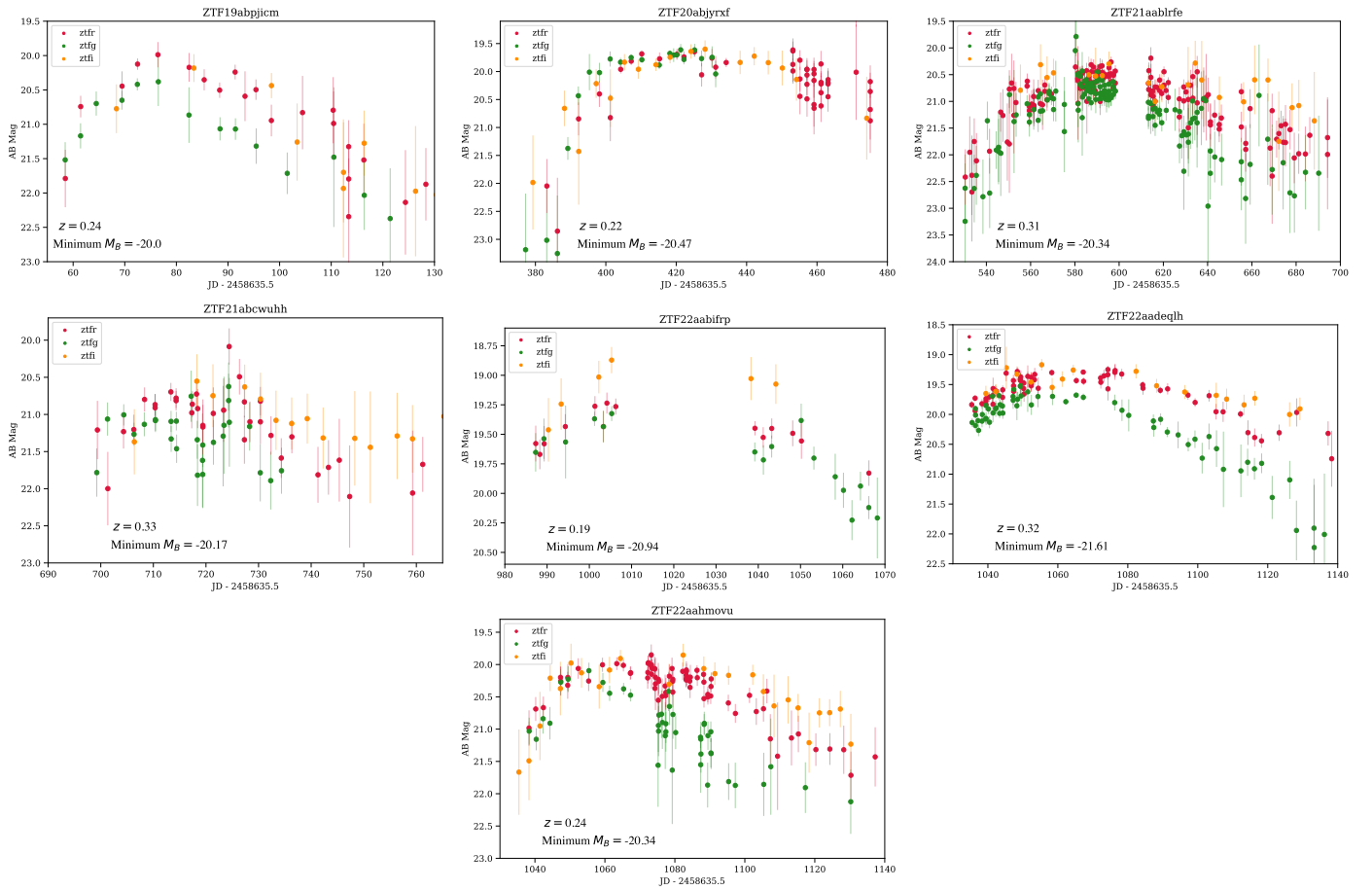


Fig. 11: Light curve plots for the seven candidates in the gold sample, that had a spectroscopic redshift from the DESI catalogue and passed all the cuts described in Sect. 4.3. Each plot shows the light curve, the lens redshift, and peak absolute magnitude at the lens redshift (from the DESI cross-match).

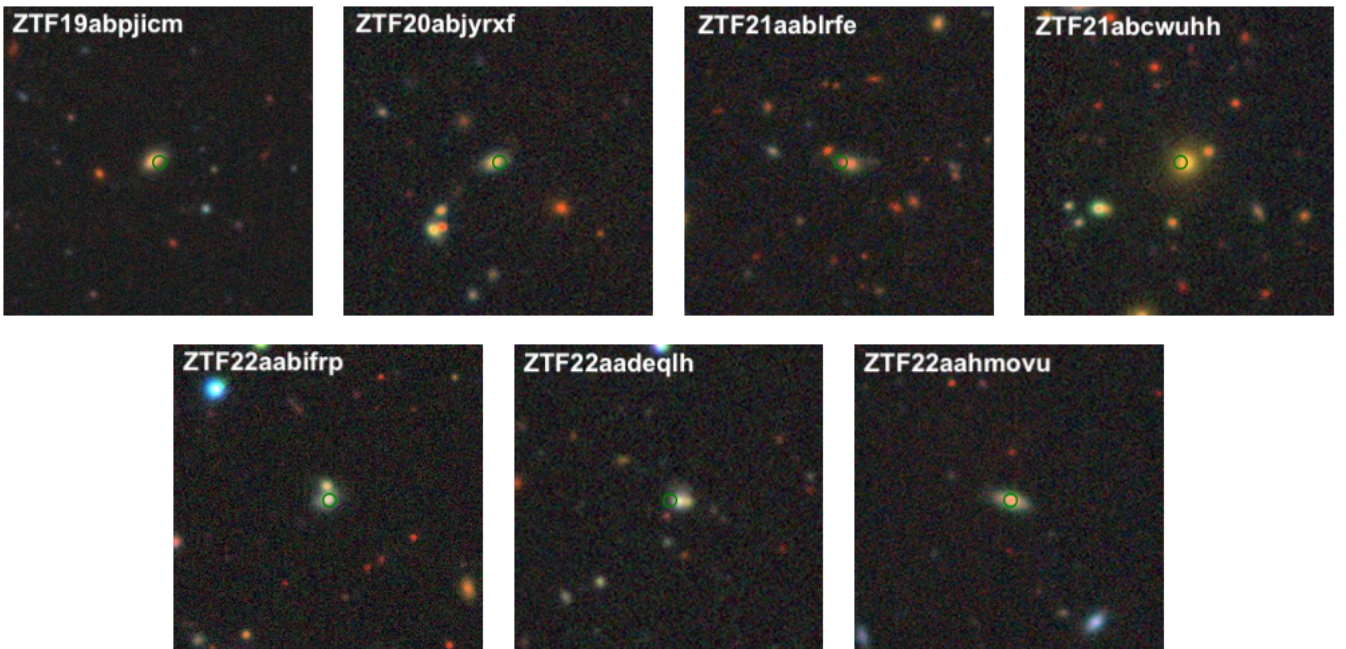


Fig. 12: Image cutouts of the LS field at the location of the transient (indicated by a green circle) for the seven gold sample candidates (the ZTF name for each transient is shown in the top left of the cutout). The galaxies we see are likely the lensing galaxies, and the host is more distant and faint.

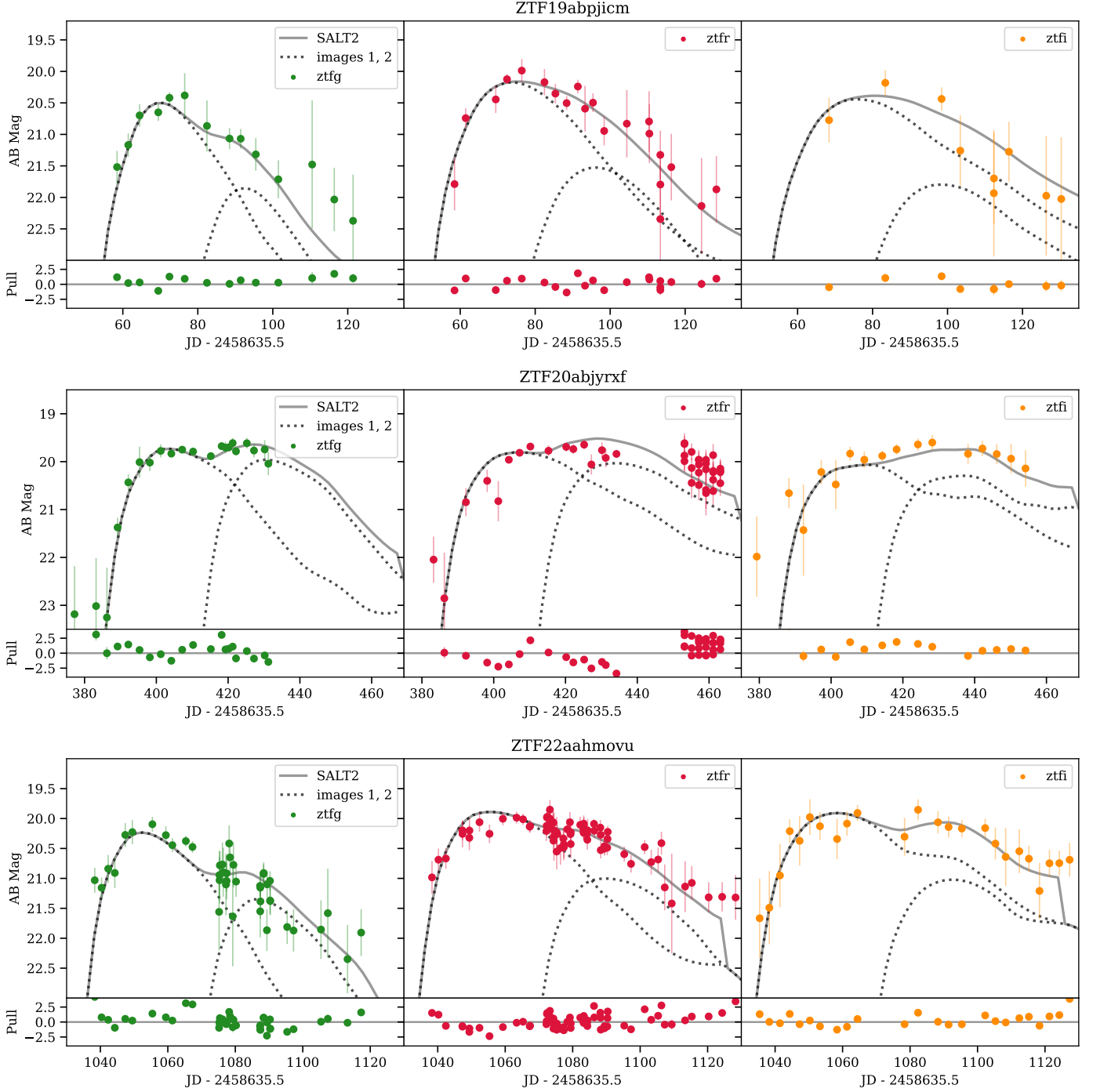


Fig. 13: Two-image combined SALT2 template fits for the three candidates in the gold sample that had a reasonable fit; ZTF19abpjicm, ZTF20abjyxf, and ZTF22aahmovu. Each plot shows the light curve in  $g$ -,  $r$ - and  $i$ -bands, the best fit combined SALT2 model (solid grey line), and the model for each lensed image (dashed grey lines). The fit parameters are given in Table 6.

for image separation, (derived from e.g. Mörtzell et al. 2020):

$$\Delta\theta = 0.27'' \sqrt{\left(\frac{\Delta t}{\text{days}}\right) \left(\frac{500 \text{ Mpc}}{2 D_l}\right) \left(\frac{D_s}{D_{ls}}\right) \frac{(r+1)}{(r-1)} \frac{1}{(1+z_l)}}, \quad (4)$$

where  $z_l$  is the lens redshift, and  $D_l$ ,  $D_s$ ,  $D_{ls}$  are the angular diameter distances to the lens, source, and between the lens and the source, respectively. Furthermore, the image separation scales with the square of the velocity dispersion,  $v$ , of the lensing

galaxy, according to the following equation:

$$\Delta\theta = 1.15'' \left(\frac{v}{200 \text{ km s}^{-1}}\right)^2. \quad (5)$$

We combined Equation 4 and 5 to calculate  $v$  in terms of our fitted parameters:

$$v = 47 \text{ km s}^{-1} \left[\left(\frac{\Delta t}{\text{days}}\right) \left(\frac{500 \text{ Mpc}}{2 D_l}\right) \left(\frac{D_s}{D_{ls}}\right) \frac{(r+1)}{(r-1)} \frac{1}{(1+z_l)}\right]^{1/4} \quad (6)$$

Table 7: Two-image combined SALT2 model parameters for the gold sample

Parameter	ZTF19abpjicm	ZTF20abjyrxf	ZTF22aahmovu
$\Delta\theta$ (")	1.1	6.7	1.7
$v$ (km s <sup>-1</sup> )	190	480	240

**Notes.** These values are heavily reliant on the source redshift and the time delays, which are unknown and only estimated by the SALT2 two-image fits.

The calculated values for  $\Delta\theta$  and  $v$  are displayed in Table 7 for the three objects with reasonable two-image combined SALT2 fits, derived from the parameters in Table 6.

### 6.2. Rise, decline and duration calculations

We calculated the time of rise, decline, and duration in the  $r$ -band for each of the seven gold sample candidates, as shown in Table 8. This is a useful characteristic to compare with contaminants like SLSNe, which typically have a larger rise time and duration. However, we note that gISNe Ia with a brighter second bump would display a longer rise and shorter decline (such as in the case of ZTF20abjyrxf in Fig. 13).

We defined the rise time as the time it takes the transient to rise from 50% of the peak flux value to the peak ( $t_{\text{peak}} - t_{50\%,r}$ ), and conversely for the decline time ( $t_{50\%,d} - t_{\text{peak}}$ ). Hence, the duration was defined as the sum of the rise and decline times. The  $r$ -band was chosen as this band usually had the most detections, due to the regular cadence and redness of the objects. For simplicity, and to avoid introducing any biases from models, we assumed that the largest flux value was the peak of the light curve. The values  $t_{50\%,r}$  and  $t_{50\%,d}$  were determined by averaging the time of detection before and after the flux values crossed the 50% threshold. If there was no detection before (or after) the 50% peak flux threshold, then the first (or last) detection date was chosen.

Table 8: Duration, rise and decline times for the gold sample

ZTF ID	Time in observer-frame (days)		
	Duration	Rise	Decline
ZTF19abpjicm	31.4	10.9	20.5
ZTF20abjyrxf	58.4	50.4	8.0
ZTF21aablrfe	72.8	63.4	9.4
ZTF21abcwuhh	18.5	12.6	5.9
ZTF22aabifrp	78.9	14.0	64.9
ZTF22aadeqlh	92.4	53.4	39.0
ZTF22aahmovu	57.5	28.4	29.1

A comparison of the duration of the gISNe Ia candidates in the gold sample to the duration of SLSNe-I and SLSNe-II from the Bright Transient Survey (Perley et al. 2020) is shown in Fig. 14. We do not see a clear distinction between our gISNe candidates and the SLSNe, but we note that the selection of candidates that had a reasonable two-image SALT2 fit displayed a shorter duration.

### 6.3. Candidate lens galaxy properties

We want to estimate the stellar masses of the gold sample candidate’s galaxies to determine whether they are consistent with SLSN host galaxies or lens galaxies. For each candidate in the

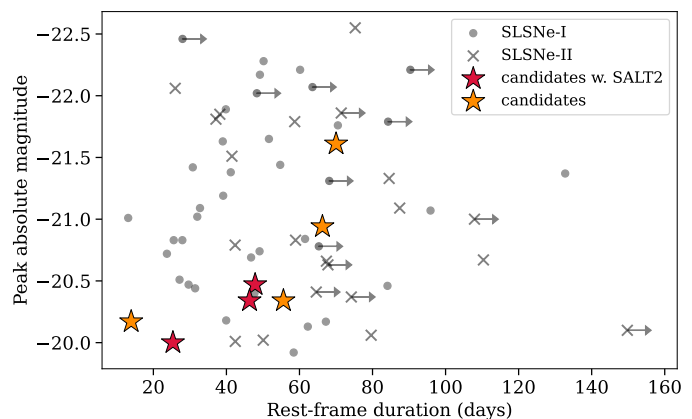


Fig. 14: A plot to compare the rest-frame duration of the seven gold candidates (red stars for candidates with a reasonable two-image SALT2 fit and gold stars for the remaining objects) with SLSNe-I and SLSNe-II from the ZTF Bright Transient Survey. In this plot, we assume that the catalogue-matched redshift for our candidates belongs to the host (which would be the case if we treated the candidates like potential SLSNe).

Table 9: Candidate lens galaxy properties of the gISNe Ia candidates in the gold sample

ZTF	$\log(M_{\star}/M_{\odot})$	SFR ( $M_{\odot} \text{ yr}^{-1}$ )
ZTF19abpjicm	$10.88^{+0.10}_{-0.30}$	$13.34^{+8.10}_{-3.86}$
ZTF20abjyrxf	$10.40^{+0.19}_{-0.39}$	$0.71^{+5.34}_{-0.69}$
ZTF21aablrfe	$10.76^{+0.13}_{-0.14}$	$19.08^{+7.66}_{-4.73}$
ZTF21abcwuhh	$11.61^{+0.11}_{-0.24}$	$1.57^{+3.36}_{-1.57}$
ZTF22aabifrp	$9.90^{+0.21}_{-0.38}$	$7.56^{+13.13}_{-4.66}$
ZTF22aadeqlh	$10.65^{+0.16}_{-0.18}$	$31.45^{+17.48}_{-12.65}$
ZTF22aahmovu	$10.71^{+0.17}_{-0.49}$	$4.48^{+11.43}_{-3.17}$

gold sample, we retrieved science-ready co-added images from the *Galaxy Evolution Explorer* GALEX general release 6/7 (Martin et al. 2005), the Sloan Digital Sky Survey DR 9 (SDSS; Ahn et al. 2012), the Panoramic Survey Telescope and Rapid Response System (Pan-STARRS, PS1) DR1 (Chambers et al. 2016), DESI Legacy Imaging Surveys (Legacy Surveys, LS) Dey et al. (2019), the Two Micron All Sky Survey (2MASS; Skrutskie et al. 2006), and images from the Wide-Field Infrared Survey Explorer (Wright et al. 2010, WISE); processed by Lang (2014). We measured the brightness of the potential lensing galaxy using LAMBDA<sup>16</sup> (Lambda Adaptive Multi-Band Deblending Algorithm in R; Wright et al. 2016) and the methods described in Schulze et al. (2021). Tables B.1 to B.7 in the Appendix display the measurements in the different bands.

We modelled the observed spectral energy distribution with the software package Prospector version 1.1 (Johnson et al. 2021)<sup>17</sup>. We assume a Chabrier IMF (Chabrier 2003) and approximate the star formation history (SFH) by a linearly increas-

<sup>16</sup> <https://github.com/AngusWright/LAMBDA>

<sup>17</sup> Prospector uses the Flexible Stellar Population Synthesis (FSPS) code (Conroy et al. 2009) to generate the underlying physical model and python-fsps (Foreman-Mackey et al. 2014) to interface with FSPS in Python. The FSPS code also accounts for the contribution from the diffuse gas based on the Cloudy models from Byler et al. (2017). We use the dynamic nested sampling package dynesty (Speagle 2020) to sample the posterior probability.

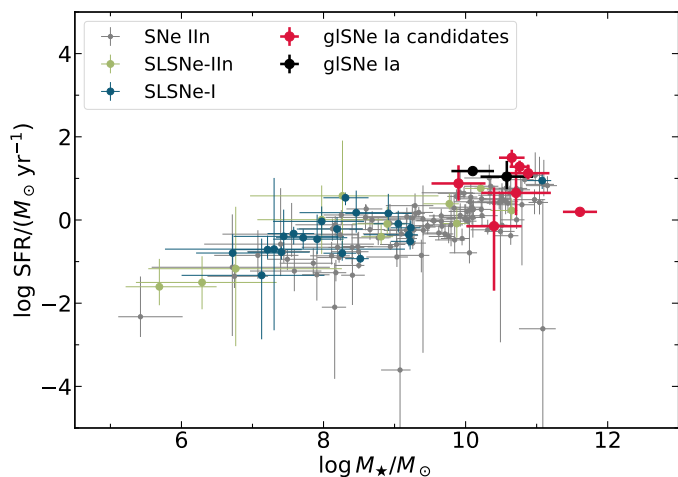


Fig. 15: The star-formation rate and stellar mass of the gISN Ia candidate lens galaxies (black), known gISNe Ia lens galaxies (red), and SLSNe-I (green), SLSNe-II (blue) and SNe IIn (grey) host galaxies. The lens galaxy of the gISN Ia candidates are similar to hosts of SLSNe-II and SNe IIn, suggesting that some gISN Ia candidates could be SLSNe-II. However, the masses are also consistent with previously observed galaxy lenses.

ing SFH at early times followed by an exponential decline at late times [functional form  $t \times \exp(-t/\tau)$ , where  $t$  is the age of the SFH episode and  $\tau$  is the  $e$ -folding timescale]. The model is attenuated with the Calzetti et al. (2000) model. The priors of the model parameters are set identically to those used by Schulze et al. (2021). Table 9 summarises the galaxy properties.

To put these measurements in context of hosts of other SN classes, we show in Fig. 15 the mass vs. star-formation rate of the candidate gISNe Ia lens galaxies and the hosts of hydrogen-poor superluminous supernovae (SLSNe-I), interaction-powered supernovae (SNe IIn) and superluminous supernovae (SLSNe-II) from the PTF survey (Schulze et al. 2021). The lens galaxies of the known gISNe Ia, SN Zwicky and iPTF16geu, are also plotted for comparison. The potential lens galaxies of the gISN Ia candidates are significantly more massive than the hosts of H-poor SLSNe, but they are consistent with the properties of SLSNe-II and SNe IIn hosts. However, they are also consistent with previously observed galaxy lenses, so we cannot exclude them as potential lensing galaxies.

## 6.4. Individual candidate discussion

### 6.4.1. ZTF19abpjcm

ZTF19abpjcm has a good two-image combined SALT2 fit (with a reduced  $\chi^2$  of 0.86), and a relatively short duration of 31.4 days. From this, we assert that the light curve is not typical for contaminants like SLSNe or TDEs.

Fitting the light curve with a single SALT2 template also produces a reasonable fit, with a larger  $x_1$  of  $2.40 \pm 0.62$  and a reduced  $\chi^2$  of 1.04, which indicates the object could be an unlensed SN Ia. The photometric and spectroscopic redshift values agree, which suggests that we can trust this object is overluminous. This means that, in the case that the object is not multiply imaged, it is not a normal SN Ia. The only Type Ia subclasses known to surpass a peak  $M_B$  of  $-20$  mag are Ia-CSM and 03fg-like. However, we do not see obvious signs of CSM interaction in the light curve (there is no plateau phase or late-time

bumps/rebrightening in the forced photometry) for a Ia-CSM and 03fg-like SN are typically bluer in the pre-peak epoch. While dust extinction could cause a redder observed colour, we estimated the attenuation that would be needed by comparing to the well-studied 03fg-like SN 2009dc (using data from the Carnegie Supernova Project; Krisciunas et al. 2017). For the  $(g-r)$  colour of ZTF19abpjcm at peak to match that of SN 2009dc, we would require an extinction of  $E(B-V) \sim 0.49$ , which corresponds to an increased brightness in the  $g$ -band of 1.9 mag. This would result in a peak  $B$ -band absolute magnitude of  $\sim -22$  mag, which is larger than the brightest observed 03fg-like SN (Ashall et al. 2021). Therefore, we conclude that it is unlikely ZTF19abpjcm is an 03fg-like SN, since the amount of dust required to match ZTF19abpjcm would imply an intrinsic brightness surpassing any observed 03fg-like SN.

From the relative magnification of the two fitted images alone, we calculated a total magnification of  $\mu_{\text{tot}} = 3.6 \pm 1.3$  in Sect. 6.1. We can also estimate the total magnification by comparing the peak apparent magnitude to the apparent magnitude we would expect from a normal SN Ia (with  $M_B = -19.4$  mag) at a redshift of 0.44 (as predicted by the combined SALT2 model). Although this requires the assumption of a cosmological model (here we assume a flat  $\Lambda$ CDM model with  $H_0 = 67.4 \text{ km s}^{-1} \text{ Mpc}^{-1}$  and  $\Omega_M = 0.315$ ; Planck Collaboration et al. 2020), and relies on the fitted redshift, it is independent of the previous method that relies solely on the flux ratios of the images. From this method, we calculate a total magnification of  $\mu_{\text{tot}} = 4.7$ . This is consistent with the  $\mu_{\text{tot}}$  estimated from the parameters of the combined SALT2 model, where the deviation is within one standard deviation ( $1\sigma$ ) of the predicted value.

Also in Sect. 6.1, we calculated an image separation ( $\Delta\theta$ ) of  $1.1''$  for the case of ZTF19abpjcm, from the estimate of the source redshift and the time delays. This is within the range of values we would expect for typical lensing systems, and agrees with our observation that the separate images were unresolved by ZTF. We also calculated a lens galaxy velocity dispersion ( $v$ ) of  $190 \text{ km s}^{-1}$ , which is typical for strong lensing galaxies with the stellar mass quoted in Table 9.

As a result, we have justified that our two-image model fit parameters are physical and consistent with our photometric measurements of the light curve and the suspected lens.

### 6.4.2. ZTF22aahmovu

ZTF22aahmovu has a good two-image combined SALT2 fit with a reduced  $\chi^2$  of 1.38. The light curve is also sufficiently red to pass the colour cuts. As a result, we assert that the light curve is not typical for SLSNe or TDEs. Additionally, the light curve does not resemble that of a normal SN Ia, so we can also exclude over-luminous Ia subclasses as being a contaminant.

From the relative magnification of the two fitted images alone, we calculated a total magnification of  $\mu_{\text{tot}} = 4.3 \pm 0.6$  in Sect. 6.1. As with ZTF19abpjcm, we also estimated the total magnification by comparing the peak apparent magnitude to the apparent magnitude we would expect from a normal SN Ia at a redshift of 0.35 (assuming the same flat  $\Lambda$ CDM cosmology). From this method, we calculate a total magnification of  $\mu_{\text{tot}} = 2.8$ . These values are consistent within three standard deviations ( $3\sigma$ ), which is reasonable when we consider that there are additional uncertainties we have not accounted for (such as microlensing by intervening stars, which could increase or decrease the magnification from the expected value).

The calculated image separation from our best-fit two-image SALT2 parameters was  $1.7''$ . We also determined a lens galaxy



velocity dispersion of  $240 \text{ km s}^{-1}$  for this system. These values are typical for strong lensing galaxies with the stellar mass quoted in Table 9.

Therefore, like with ZTF19abpjcm, we have justified that our two-image model fit parameters are physical and consistent with our photometric measurements of the light curve and the suspected lens.

#### 6.4.3. ZTF20abjyxf

ZTF20abjyxf also has a two-image combined SALT2 fit (with a reduced  $\chi^2$  of 2.53). The model displays a slight decrease in the  $g$ -band brightness as the fit transitions from being dominated by the first image to the second, which is consistent with what we observe in the light curve. Additionally, the light curve is broad with a slower rise time (approximately 58.4 days). This is attributed to the relatively equal flux contributions from the two images, which causes the peak of the model to occur later (at the peak of the second image). Nevertheless, this slower rise/plateauing feature could be characteristic of a SLSN light curve. From Fig. 15 in Sect. 6.3, the galaxy associated with ZTF20abjyxf could be consistent with the host of a SLSN-II(n).

In Sect. 6.1, we estimated a total magnification of  $\mu_{\text{tot}} = 20.4 \pm 6.2$ . This is quite large, similar to the magnification we observed from SN Zwicky (with  $\mu_{\text{tot}} = 24.3 \pm 2.7$ ). For this to be correct, we would expect the source redshift to be  $\sim 2.8$  times the value of the lens redshift (assuming the same flat  $\Lambda$ CDM cosmology as for ZTF19abpjcm), which is possible, although not consistent with the best-fit redshift parameter from the SALT2 two-image fit. We would also expect larger image separation for ZTF20abjyxf, although this is heavily dependent on the source redshift (it could vary from  $2.5''$  for  $z_s = 2.3 z_l$ , to  $6.7''$  for  $z_s = 0.24$  as determined from the SALT2 fit). Considering that the spatial resolution of ZTF is approximately  $1''$  (combined with the  $2''$  seeing at Palomar Observatory), it should be possible to distinguish the separate images in the case of a  $6.7''$  separation. However, we do not find any evidence of spatial variability in the ZTF alert images.

It is also possible that our simplified lens model does not accurately resemble the system of ZTF20abjyxf. This has been observed before; in the case of SN Zwicky, the observed relative flux contributions for two out of the four of the images did not agree with the model predictions. Furthermore, we cannot ignore the possibility that four images could be present in our case, which would change the relative image magnifications and the resulting flux ratios. As a result, we conclude that, if ZTF20abjyxf is a gLSN Ia, it is not well described by a simple two-image system with a SIS lens, and further study of the potential lens galaxy is required.

#### 6.4.4. ZTF21aablrfe

It was not possible to fit ZTF21aablrfe with a reasonable two-image SALT2 model, due to the width of the light curve and the longer rise time (approximately 60 days). It also had a poor fit to the single image SALT2 model (with a reduced  $\chi^2$  of 4.7). Additionally, it is further away from the DESI galaxy, at a separation of  $2.4''$ . The combination of these characteristics suggests that this object could be a SLSN-II(n) candidate.

Despite this, the light curve is sufficiently red to pass the colour cuts and the galaxy counterpart is not consistent with the hosts of SLSNe-I (as shown in Fig. 15). A four-image SALT2 model might be able to more accurately match the light curve

we observe, although this would require us to know more about the lens system.

#### 6.4.5. ZTF22aabifrp

ZTF22aabifrp has an interesting LS cutout, which shows two galaxies close together (less than three arcseconds apart). The DESI catalogue-matched redshift ( $z = 0.19$ ) belongs to the object above the green circle plotted in Fig. 11. The photometric redshift for the lower galaxy, which is closer to ZTF22aabifrp at a separation of  $0.1''$ , is given as  $z = 0.25 \pm 0.04$  in the LS DR9 catalogue. Therefore, the  $z = 0.19$  object may be a lens for the host at  $z = 0.25$ .

Similarly to ZTF21aablrfe, it was not possible to fit ZTF22aabifrp with a reasonable two-image SALT2 model, due to the width of the light curve. From our fit, we would expect to see two distinct peaks for the separate images, however, there is no evidence for this in the data (unfortunately, there is a large period of no observations where the valley between the two peaks would be). This is another case where a four-image SALT2 model might be able to more accurately match the light curve we observe. Also like ZTF21aablrfe, the light curve is sufficiently red to pass the colour cuts and the closest galaxy is not consistent with the hosts of SLSNe-I. Despite this, we cannot exclude the possibility that this object is a SLSN-II(n).

#### 6.4.6. ZTF22aadeqlh

The LS cutout for ZTF22aadeqlh in Fig. 12 displays two possible galaxy lenses/hosts (a larger blob to the left and a yellowish blob to the right). It is not certain which galaxy is the lens/host, although it appears that the transient is more aligned with the object on the left. The two galaxies are at approximately the same redshift according to DESI ( $z = 0.32$ ), so they may be a combined two-galaxy lens.

ZTF22aadeqlh was reported to be a candidate SLSN by Gkini et al. (2022) in an AstroNote. This is possible, because of the broad light curve and lack of a reasonable two-image SALT2 fit. Similarly to ZTF21aablrfe and ZTF22aabifrp, the light curve is sufficiently red to pass the colour cuts and the closest galaxy is not consistent with the hosts of SLSNe-I. However, once again we cannot exclude the possibility that this object is a SLSN-II(n).

#### 6.4.7. ZTF21abcwuhh

ZTF21abcwuhh has a single-image SALT2 fit with a reduced  $\chi^2$  of 1.0. However, the light curve is too faint (and, therefore, too noisy) to provide a convincing two-image combined SALT2 fit. The photometric and spectroscopic redshift values agree, which suggests that we can trust this object is over-luminous. ZTF21abcwuhh may be a gLSN Ia candidate, but the limited data means that we cannot deduce further about the true nature of this faint transient.

### 6.5. Summary of gold sample candidates

We present two candidates, ZTF19abpjcm and ZTF22aahmovu, as likely gLSNe Ia. The observed characteristics of the two objects are not typical for contaminants like SLSNe, TDEs, or over-luminous SN Ia subclasses. They can also be well-modelled by a two-image combined SALT2 fit, and the resulting parameters are consistent with our photometric measurements and adhere to the expected physical characteristics of lensing systems.

An additional candidate, ZTF20abjyxf, was also well-modelled by a two-image combined SALT2 fit. However, the resulting parameters suggest that we should have observed a larger image separation (and, therefore, should have observed the two images as separate sources in ZTF). As this was not the case, we conclude that ZTF20abjyxf is not well described by a simple two-image system with an SIS lens. Further study of the potential lens galaxy is required for us to present ZTF20abjyxf as a likely gISN Ia.

ZTF21aablrfe, ZTF22aabifrp, and ZTF22aadeqlh were not well-modelled by a two-image combined SALT2 fit because of the width of their light curves (we only see evidence for a single peak in the data, however, the model predicts that we should see two distinct peaks). Despite this, we see evidence of two galaxies at different redshifts (a potential lens and host) in the LS cutout for ZTF22aabifrp. We also observe two galaxies at approximately the same redshift for ZTF22aadeqlh, which could be a combined two-galaxy lens. As a result, we conclude that these candidates are not well described by a simple two-image system with an SIS lens, but a more complex model (e.g. with four images) could potentially provide a more accurate fit to the observed data. As with ZTF20abjyxf, follow-up of the potential lens/host galaxies is required.

## 7. Conclusions

In this work, we presented a systematic search of the ZTF archival data between 1 June 2019 and 1 September 2022 for strongly-lensed Type Ia supernovae. We created an analysis pipeline using the AMPEL processing platform, which allowed us to query the ZTF alert photometry, apply filters for SN-like objects, and perform SALT2 template fits. Then, we applied some initial cuts and acquired forced photometry for the remaining candidates. Finally, we narrowed down our most likely candidates through two selection methods; by cross-matching to the DESI spectroscopic redshift catalogues, or by applying stricter cuts motivated by simulations and previous observations. Additionally, we performed a similar analysis on the ZTF Bright Transient Survey sample of supernovae, to estimate the amount of contamination we should expect from each class.

The conclusions from our analysis and plans for future work are as follows:

1. We have shown that it is possible to filter the alert photometry of a large optical survey to find transients that match the expected characteristics of gISNe Ia. We devised an initial filtering algorithm to reduce 31930 SN-like alerts to 7075 candidates that passed some preliminary cuts. We reduced the 7075 initial candidates to 50 final gISN Ia candidates by applying additional cuts and matching to the DESI spectroscopic catalogue.
2. 27 of these final candidates were the result of a DESI cross-match (spectroscopic sample) and 27 were the result of applying stricter cuts based on simulations (photometric sample). A careful inspection of each of the spectroscopic candidates is necessary to exclude the possibility that they are SLSNe. Both the spectroscopic and photometric samples will be targeted in future spectroscopic follow-up missions to determine the lens and/or host redshifts.
3. The vast majority of the final candidates were found within the lens redshift range of  $0.2 < z < 0.4$ . Additionally, they were all dimmer than SN Zwicky and iPTF16geu, which suggests that, if they are truly gISNe Ia, they would belong to a less magnified population.

4. Seven candidates were present in both the spectroscopic and photometric samples, and these were discussed in more depth in this work. We present two candidates, ZTF19abpjcm and ZTF22aahmovu, as likely gISNe Ia. They are well-modelled by a combined two-image SALT2 template and the model fit parameters are consistent with the physical parameters we would expect for strong lensing systems. From this two-image modelling, we estimate time delays of  $22 \pm 3$  and  $34 \pm 1$  days for the two events, respectively, which suggests that we have uncovered a population of gISNe Ia with longer time delays. The remaining five objects are still promising candidate gISNe Ia, but we would require more information about their lensing systems to more accurately model them.
5. The two most promising candidates, ZTF19abpjcm and ZTF22aahmovu, should be targeted in a follow-up program to confirm that they occurred in a strong lensing system. To do this, we suggest acquiring high-resolution photometry of the system, to search for evidence of a strongly-lensed background host galaxy. Alternatively, if the host galaxy is not lensed, we suggest acquiring deeper spectra of the potential lens galaxy, to search for additional lines from a background host galaxy.

In this paper, we have highlighted the importance of lensed transients (particularly standardisable candles like SNe Ia) for cosmology and presented a pipeline that is both efficient and sensitive enough to parse full alert streams from optical observatories to search for gISNe Ia. The methodology presented in this systematic search is currently applied as a live search in ZTF, and it could be the foundation for future live searches in LSST and beyond. To fully remove the sources of contamination, spectroscopic follow-up while the transient is live is necessary. Despite this, we have shown that it is still possible to eliminate contaminants based on light curve modelling and photometric observations of the galaxy counterpart, and, as a result, we present two likely gISNe Ia.

## 8. Data availability

All ZTF light curve data is publicly available at <https://www.ztf.caltech.edu/ztf-public-releases.html>. The instructions for how to install and run the AMPEL platform can be found at <https://github.com/AmpelAstro/Ampel-HU-astro/>. The specific AMPEL workflow we used to obtain the alert photometry, cross-match to galaxy catalogues, and perform initial filtering is found at [https://github.com/AmpelAstro/Ampel-HU-astro/blob/main/notebooks/run\\_lensing\\_query.ipynb](https://github.com/AmpelAstro/Ampel-HU-astro/blob/main/notebooks/run_lensing_query.ipynb). The forced photometry pipeline for ZTF data that we utilised can be found at <https://github.com/simeonreusch/fpbot>. The BTS sample, which we utilised to estimate the contaminants present in our sample, is publicly accessible at <https://sites.astro.caltech.edu/ztf/bts/explorer.php>. All external data sources are referenced in the main text. Supplemental data are accessible at <https://zenodo.org/records/11105340>.

*Acknowledgements.* Based on observations obtained with the Samuel Oschin Telescope 48-inch and the 60-inch Telescope at the Palomar Observatory as part of the Zwicky Transient Facility project. ZTF is supported by the National Science Foundation under Grants No. AST-1440341 and AST-2034437 and a collaboration including current partners Caltech, IPAC, the Weizmann Institute of Science, the Oskar Klein Center at Stockholm University, the University of Maryland, Deutsches Elektronen-Synchrotron and Humboldt University, the TANGO Consortium of Taiwan, the University of Wisconsin at Milwaukee, Trinity College Dublin, Lawrence Livermore National Laboratories, IN2P3, University of Warwick, Ruhr University Bochum, Northwestern University and former

partners the University of Washington, Los Alamos National Laboratories, and Lawrence Berkeley National Laboratories. Operations are conducted by COO, IPAC, and UW.

This work has been supported by the research project grant “Understanding the Dynamic Universe” funded by the Knut and Alice Wallenberg Foundation under Dnr KAW 2018.0067, *Vetenskapsrådet*, the Swedish Research Council, project 2020-03444, and the G.R.E.A.T research environment, project number 2016-06012.

This material is based upon work supported by the U.S. Department of Energy (DOE), Office of Science, Office of High-Energy Physics, under Contract No. DE-AC02-05CH11231, and by the National Energy Research Scientific Computing Center, a DOE Office of Science User Facility under the same contract. Additional support for DESI was provided by the U.S. National Science Foundation (NSF), Division of Astronomical Sciences under Contract No. AST-0950945 to the NSF’s National Optical-Infrared Astronomy Research Laboratory; the Science and Technology Facilities Council of the United Kingdom; the Gordon and Betty Moore Foundation; the Heising-Simons Foundation; the French Alternative Energies and Atomic Energy Commission (CEA); the National Council of Science and Technology of Mexico (CONACYT); the Ministry of Science and Innovation of Spain (MICINN), and by the DESI Member Institutions: <https://www.desi.lbl.gov/collaborating-institutions>. Any opinions, findings, and conclusions or recommendations expressed in this material are those of the author(s) and do not necessarily reflect the views of the U. S. National Science Foundation, the U. S. Department of Energy, or any of the listed funding agencies.

The authors are honored to be permitted to conduct scientific research on Iolkam Du’ag (Kitt Peak), a mountain with particular significance to the Tohono O’odham Nation.

S. Schulze is partially supported by LBNL Subcontract NO. 7707915.

M. W. Coughlin acknowledges support from the National Science Foundation with grant numbers PHY-2308862 and PHY-2117997.

## References

- Ahn, C. P., Alexandroff, R., Allende Prieto, C., et al. 2012, *ApJS*, 203, 21
- Arendse, N., Dhawan, S., Sagués Carracedo, A., et al. 2023, arXiv e-prints, arXiv:2312.04621
- Ashall, C., Lu, J., Hsiao, E. Y., et al. 2021, *ApJ*, 922, 205
- Assef, R. J., Stern, D., Noirot, G., et al. 2018, *ApJS*, 234, 23
- Bag, S., Kim, A. G., Linder, E. V., & Shafieloo, A. 2021, *ApJ*, 910, 65
- Barbary, K., Bailey, S., Barentsen, G., et al. 2022, *SNCosmo*
- Beck, R., Szapudi, I., Flewelling, H., et al. 2021, *MNRAS*, 500, 1633
- Bellm, E. C., Kulkarni, S. R., Barlow, T., et al. 2019a, *PASP*, 131, 068003
- Bellm, E. C., Kulkarni, S. R., Graham, M. J., et al. 2019b, *PASP*, 131, 018002
- Betoule, M., Kessler, R., Guy, J., et al. 2014, *A&A*, 568, A22
- Bilicki, M., Jarrett, T. H., Peacock, J. A., Cluver, M. E., & Steward, L. 2014, *ApJS*, 210, 9
- Bilicki, M., Peacock, J. A., Jarrett, T. H., et al. 2016, *ApJS*, 225, 5
- Birrer, S., Dhawan, S., & Shajib, A. J. 2022, *ApJ*, 924, 2
- Blagorodnova, N., Neill, J. D., Walters, R., et al. 2018, *PASP*, 130, 035003
- Brescia, M., Cavuoti, S., & Longo, G. 2015, *MNRAS*, 450, 3893
- Byler, N., Dalcanton, J. J., Conroy, C., & Johnson, B. D. 2017, *ApJ*, 840, 44
- Calzetti, D., Armus, L., Bohlin, R. C., et al. 2000, *ApJ*, 533, 682
- Chabrier, G. 2003, *PASP*, 115, 763
- Chambers, K. C., Magnier, E. A., Metcalfe, N., et al. 2016, arXiv e-prints, arXiv:1612.05560
- Chornock, R., Berger, E., Rest, A., et al. 2013, *ApJ*, 767, 162
- Collett, T. E. 2015, *ApJ*, 811, 20
- Conroy, C., Gunn, J. E., & White, M. 2009, *ApJ*, 699, 486
- Craig, P., O’Connor, K., Chakrabarti, S., et al. 2021, arXiv e-prints, arXiv:2111.01680
- Dálya, G., Galgóczi, G., Dobos, L., et al. 2018, *MNRAS*, 479, 2374
- Dekany, R., Smith, R. M., Riddle, R., et al. 2020, *PASP*, 132, 038001
- Denissenya, M., Bag, S., Kim, A. G., Linder, E. V., & Shafieloo, A. 2022, *MNRAS*, 511, 1210
- DESI Collaboration, Abareshi, B., Aguilar, J., et al. 2022, *AJ*, 164, 207
- DESI Collaboration, Adame, A. G., Aguilar, J., et al. 2023, arXiv e-prints, arXiv:2306.06308
- DESI Collaboration, Adame, A. G., Aguilar, J., et al. 2024a, *AJ*, 167, 62
- DESI Collaboration, Adame, A. G., Aguilar, J., et al. 2024b, arXiv e-prints, arXiv:2404.03002
- DESI Collaboration, Adame, A. G., Aguilar, J., et al. 2024c, arXiv e-prints, arXiv:2404.03001
- DESI Collaboration, Adame, A. G., Aguilar, J., et al. 2024d, arXiv e-prints, arXiv:2404.03000
- DESI Collaboration, Aghamousa, A., Aguilar, J., et al. 2016a, arXiv e-prints, arXiv:1611.00036
- DESI Collaboration, Aghamousa, A., Aguilar, J., et al. 2016b, arXiv e-prints, arXiv:1611.00037
- Dey, A., Schlegel, D. J., Lang, D., et al. 2019, *AJ*, 157, 168
- Duncan, K. J. 2022, *MNRAS*, 512, 3662
- Falco, E. E., Gorenstein, M. V., & Shapiro, I. I. 1985, *ApJ*, 289, L1
- Foreman-Mackey, D., Sick, J., & Johnson, B. 2014, *Python-Fsps: Python Bindings To Fsps (V0.1.1)*
- Fremming, C., Miller, A. A., Sharma, Y., et al. 2020, *ApJ*, 895, 32
- Frye, B. L., Pascale, M., Pierel, J., et al. 2023, arXiv e-prints, arXiv:2309.07326
- Gkini, A., Yan, L., Perley, D. A., et al. 2022, *Transient Name Server AstroNote*, 124, 1
- Goldstein, D. A. & Nugent, P. E. 2017, *ApJ*, 834, L5
- Goldstein, D. A., Nugent, P. E., & Goobar, A. 2019, *ApJS*, 243, 6
- Goobar, A., Amanullah, R., Kulkarni, S. R., et al. 2017, *Science*, 356, 291
- Goobar, A., Johansson, J., Schulze, S., et al. 2023, *Nature Astronomy* [arXiv:2211.00656]
- Goobar, A., Mörtzell, E., Amanullah, R., & Nugent, P. 2002, *A&A*, 393, 25
- Goobar, A., Paech, K., Stanishev, V., et al. 2009, *A&A*, 507, 71
- Graham, M. J., Kulkarni, S. R., Bellm, E. C., et al. 2019, *PASP*, 131, 078001
- Guy, J., Astier, P., Baumont, S., et al. 2007, *A&A*, 466, 11
- Guy, J., Bailey, S., Kremin, A., et al. 2023, *AJ*, 165, 144
- Hahn, C., Wilson, M. J., Ruiz-Macias, O., et al. 2023, *AJ*, 165, 253
- Howell, D. A., Sullivan, M., Nugent, P. E., et al. 2006, *Nature*, 443, 308
- Ivezić, Ž., Kahn, S. M., Tyson, J. A., et al. 2019, *ApJ*, 873, 111
- Johansson, J., Goobar, A., Price, S. H., et al. 2021, *MNRAS*, 502, 510
- Johnson, B. D., Leja, J., Conroy, C., & Speagle, J. S. 2021, *ApJS*, 254, 22
- Kelly, P. L., Rodney, S. A., Treu, T., et al. 2015, *Science*, 347, 1123
- Krisciunas, K., Contreras, C., Burns, C. R., et al. 2017, *AJ*, 154, 211
- Lang, D. 2014, *AJ*, 147, 108
- Leloudas, G., Schulze, S., Krühler, T., et al. 2015, *MNRAS*, 449, 917
- Levi, M., Bebek, C., Beers, T., et al. 2013, arXiv e-prints, arXiv:1308.0847
- Lunnan, R., Chornock, R., Berger, E., et al. 2014, *ApJ*, 787, 138
- Magee, M. R., Sainz de Murieta, A., Collett, T. E., & Enzi, W. 2023, *MNRAS*, 525, 542
- Martin, D. C., Fanson, J., Schiminovich, D., et al. 2005, *ApJ*, 619, L1
- Masci, F. J., Laher, R. R., Rusholme, B., et al. 2019, *PASP*, 131, 018003
- Miller, T. N., Doel, P., Gutierrez, G., et al. 2023, arXiv e-prints, arXiv:2306.06310
- Millon, M., Galan, A., Courbin, F., et al. 2020, *A&A*, 639, A101
- Mörtzell, E., Johansson, J., Dhawan, S., et al. 2020, *MNRAS*, 496, 3270
- Nordin, J., Brinnet, V., van Santen, J., et al. 2019, *A&A*, 631, A147
- Nordin, J., Rubin, D., Richard, J., et al. 2014, *MNRAS*, 440, 2742
- Patel, B., McCully, C., Jha, S. W., et al. 2014, *ApJ*, 786, 9
- Patterson, M. T., Bellm, E. C., Rusholme, B., et al. 2019, *PASP*, 131, 018001
- Perley, D. A., Fremming, C., Sollerman, J., et al. 2020, *ApJ*, 904, 35
- Petrushevska, T., Amanullah, R., Bulla, M., et al. 2017, *A&A*, 603, A136
- Petrushevska, T., Amanullah, R., Goobar, A., et al. 2016, *A&A*, 594, A54
- Pierel, J. D. R., Arendse, N., Ertl, S., et al. 2023, *ApJ*, 948, 115
- Planck Collaboration, Aghanim, N., Akrami, Y., et al. 2020, *A&A*, 641, A6
- Quimby, R. M., Oguri, M., More, A., et al. 2014, *Science*, 344, 396
- Quimby, R. M., Werner, M. C., Oguri, M., et al. 2013, *ApJ*, 768, L20
- Refsdal, S. 1964, *MNRAS*, 128, 307
- Reusch, S. 2023, *simeonreusch/fpbot: Release 1.1.2*
- Reusch, S., Stein, R., Kowalski, M., et al. 2022, *Phys. Rev. Lett.*, 128, 221101
- Rodney, S. A., Brammer, G. B., Pierel, J. D. R., et al. 2021, *Nature Astronomy*, 5, 1118
- Rodney, S. A., Patel, B., Scolnic, D., et al. 2015, *ApJ*, 811, 70
- Saini, T. D., Raychaudhury, S., & Shchekinov, Y. A. 2000, *A&A*, 363, 349
- Sainz de Murieta, A., Collett, T. E., Magee, M. R., et al. 2023, *MNRAS*, 526, 4296
- Schulze, S., Krühler, T., Leloudas, G., et al. 2018, *MNRAS*, 473, 1258
- Schulze, S., Yaron, O., Sollerman, J., et al. 2021, *ApJS*, 255, 29
- Shajib, A. J., Birrer, S., Treu, T., et al. 2020, *MNRAS*, 494, 6072
- Sharma, Y., Sollerman, J., Fremming, C., et al. 2023, *ApJ*, 948, 52
- Shu, Y., Bolton, A. S., Mao, S., et al. 2018, *ApJ*, 864, 91
- Silber, J. H., Fagrellius, P., Fanning, K., et al. 2023, *AJ*, 165, 9
- Skrutskie, M. F., Cutri, R. M., Stiening, R., et al. 2006, *AJ*, 131, 1163
- Sonnenfeld, A., Verma, A., More, A., et al. 2020, *VizieR Online Data Catalog*, J/A+A/642/A148
- Soumagnac, M. T. & Ofek, E. O. 2018, *PASP*, 130, 075002
- Speagle, J. S. 2020, *MNRAS*, 493, 3132
- Sullivan, M., Ellis, R., Nugent, P., Smail, I., & Madau, P. 2000, *MNRAS*, 319, 549
- Wojtak, R., Hjorth, J., & Gall, C. 2019, *MNRAS*, 487, 3342
- Wong, K. C., Suyu, S. H., Chen, G. C. F., et al. 2020, *MNRAS*, 498, 1420
- Wright, A. H., Robotham, A. S. G., Bourne, N., et al. 2016, *MNRAS*, 460, 765
- Wright, E. L., Eisenhardt, P. R. M., Mainzer, A. K., et al. 2010, *AJ*, 140, 1868
- Yang, J., Wang, L., Suntzeff, N., et al. 2022, *ApJ*, 938, 83
- Yao, Y., Somalwar, J., Hammerstein, E., et al. 2022, *Transient Name Server Classification Report*, 2022-925, 1

- 
- <sup>1</sup> Institut für Physik, Humboldt-Universität zu Berlin, Newtonstr. 15, D-12489 Berlin, Germany
- <sup>2</sup> Oskar Klein Centre, Department of Physics, Stockholm University, Albanova University Center, SE 106 91 Stockholm, Sweden
- <sup>3</sup> Deutsches Elektronen-Synchrotron, D-15735 Zeuthen, Germany
- <sup>4</sup> Institute of Astronomy and Kavli Institute for Cosmology, University of Cambridge, Madingley Road, Cambridge CB3 0HA, UK
- <sup>5</sup> Center for Interdisciplinary Exploration and Research in Astrophysics (CIERA), Northwestern University, 1800 Sherman Ave., Evanston, IL 60201, USA
- <sup>6</sup> Joint Space-Science Institute, University of Maryland, College Park, MD 20742, USA
- <sup>7</sup> Department of Astronomy, University of Maryland, College Park, MD 20742, USA
- <sup>8</sup> Astrophysics Science Division, NASA Goddard Space Flight Center, Mail Code 661, Greenbelt, MD 20771, USA
- <sup>9</sup> Instituto de Astrofísica de Andalucía (CSIC), Glorieta de la Astronomía, s/n, E-18008 Granada, Spain
- <sup>10</sup> Lawrence Berkeley National Laboratory, 1 Cyclotron Road, Berkeley, CA 94720, USA
- <sup>11</sup> Department of Astronomy, University of California, Berkeley, 501 Campbell Hall, Berkeley, CA 94720, USA
- <sup>12</sup> Univ Lyon, Univ Claude Bernard Lyon 1, CNRS, IP2I Lyon/IN2P3, UMR 5822, F-69622, Villeurbanne, France
- <sup>13</sup> Nordita, Stockholm University and KTH Royal Institute of Technology, Hannes Alfvéns väg 12, SE-106 91 Stockholm, Sweden
- <sup>14</sup> DIRAC Institute, Department of Astronomy, University of Washington, 3910 15th Avenue NE, Seattle, WA 98195, USA
- <sup>15</sup> School of Physics and Astronomy, University of Minnesota, Minneapolis, Minnesota 55455, USA
- <sup>16</sup> Caltech Optical Observatories, California Institute of Technology, Pasadena, CA 91125, USA
- <sup>17</sup> IPAC, California Institute of Technology, 1200 E. California Boulevard, Pasadena, CA 91125, USA
- <sup>18</sup> LPNHE, CNRS/IN2P3, Sorbonne Université, Laboratoire de Physique Nucléaire et de Hautes Énergies, F-75005 Paris, France
- <sup>19</sup> Physics Dept., Boston University, 590 Commonwealth Avenue, Boston, MA 02215, USA
- <sup>20</sup> Department of Physics & Astronomy, University College London, Gower Street, London, WC1E 6BT, UK
- <sup>21</sup> Instituto de Física, Universidad Nacional Autónoma de México, Cd. de México C.P. 04510, México
- <sup>22</sup> NSF's NOIRLab, 950 N. Cherry Ave., Tucson, AZ 85719, USA
- <sup>23</sup> Department of Physics & Astronomy and Pittsburgh Particle Physics, Astrophysics, and Cosmology Center (PITT PACC), University of Pittsburgh, 3941 O'Hara Street, Pittsburgh, PA 15260, USA
- <sup>24</sup> Kavli Institute for Particle Astrophysics and Cosmology, Stanford University, Menlo Park, CA 94305, USA
- <sup>25</sup> SLAC National Accelerator Laboratory, Menlo Park, CA 94305, USA
- <sup>26</sup> Departamento de Física, Universidad de los Andes, Cra. 1 No. 18A-10, Edificio Ip, CP 111711, Bogotá, Colombia
- <sup>27</sup> Observatorio Astronómico, Universidad de los Andes, Cra. 1 No. 18A-10, Edificio H, CP 111711 Bogotá, Colombia
- <sup>28</sup> Institut d'Estudis Espacials de Catalunya (IEEC), 08034 Barcelona, Spain
- <sup>29</sup> Institute of Cosmology and Gravitation, University of Portsmouth, Dennis Sciama Building, Portsmouth, PO1 3FX, UK
- <sup>30</sup> Institute of Space Sciences, ICE-CSIC, Campus UAB, Carrer de Can Magrans s/n, 08913 Bellaterra, Barcelona, Spain
- <sup>31</sup> Center for Cosmology and AstroParticle Physics, Ohio State University, 191 West Woodruff Avenue, Columbus, OH 43210, USA
- <sup>32</sup> Department of Physics, Ohio State University, 191 West Woodruff Avenue, Columbus, OH 43210, USA
- <sup>33</sup> The Ohio State University, Columbus, 43210 OH, USA
- <sup>34</sup> School of Mathematics and Physics, University of Queensland, 4072, Australia
- <sup>35</sup> Departament de Física, Serra Hünter, Universitat Autònoma de Barcelona, 08193 Bellaterra, Barcelona, Spain
- <sup>36</sup> Institut de Física d'Altes Energies (IFAE), Barcelona Institute of Science and Technology, Campus UAB, 08193 Bellaterra, Barcelona, Spain
- <sup>37</sup> Institució Catalana de Recerca i Estudis Avançats, Passeig de Lluís Companys, 23, 08010 Barcelona, Spain
- <sup>38</sup> Department of Physics and Astronomy, Siena College, 515 Loudon Road, Loudonville, NY 12211, USA
- <sup>39</sup> Department of Physics and Astronomy, University of Sussex, Brighton BN1 9QH, UK
- <sup>40</sup> Department of Physics & Astronomy, University of Wyoming, 1000 E. University, Dept. 3905, Laramie, WY 82071, USA
- <sup>41</sup> National Astronomical Observatories, Chinese Academy of Sciences, A20 Datun Rd., Chaoyang District, Beijing, 100012, P.R. China
- <sup>42</sup> IRFU, CEA, Université Paris-Saclay, F-91191 Gif-sur-Yvette, France
- <sup>43</sup> Space Sciences Laboratory, University of California, Berkeley, 7 Gauss Way, Berkeley, CA 94720, USA
- <sup>44</sup> Department of Physics, Kansas State University, 116 Cardwell Hall, Manhattan, KS 66506, USA
- <sup>45</sup> Department of Physics and Astronomy, Sejong University, Seoul, 143-747, Korea
- <sup>46</sup> CIEMAT, Avenida Complutense 40, E-28040 Madrid, Spain
- <sup>47</sup> Department of Physics, University of Michigan, Ann Arbor, MI 48109, USA
- <sup>48</sup> University of Michigan, Ann Arbor, MI 48109, USA
- <sup>49</sup> Department of Physics & Astronomy, Ohio University, Athens, OH 45701, USA

## Appendix A: Data for candidates that passed selection criteria

Table A.1 details the measured parameters of the 125 candidates that passed the selection criteria in Sects. 4.2 and 4.3, before the final visual inspection phase. This includes the ZTF ID, right ascension (RA), declination (dec.), photometric redshift (phot.  $z$ ), DESI redshift, angular separation from the catalogue counterpart (ang. sep.) for both the photometric and DESI redshifts, peak absolute  $B$ -band magnitude from SALT2 (for both the photometric and DESI redshifts), SALT2  $x_1$  and associated error, SALT2  $c$  and associated error, whether it passed selection method 1 with DESI cross-matching (detailed in Sect. 4.2) and/or selection method 2 with additional cuts (detailed in Sect. 4.3), and the reason it was rejected from the final candidate sample (if any).

## Appendix B: Galaxy photometry of gold sample candidates

Tables B.1 to B.7 show the photometry we acquired for the potential lens/host galaxies of the seven candidates in the gold sample (as described in Sect. 6.3). From this photometry, we calculated the stellar masses and star formation rate for each candidate.

Table B.1: Host photometry of ZTF19abpjicm

ZTF19abpjicm	
GALEX/ <i>FUV</i>	$22.92 \pm 0.42$
GALEX/ <i>NUV</i>	$21.35 \pm 0.14$
SDSS/ <i>u</i>	$21.15 \pm 0.60$
SDSS/ <i>g</i>	$20.14 \pm 0.06$
SDSS/ <i>i</i>	$18.56 \pm 0.05$
SDSS/ <i>r</i>	$19.10 \pm 0.03$
SDSS/ <i>z</i>	$18.07 \pm 0.10$
PS1/ <i>g</i>	$19.97 \pm 0.15$
PS1/ <i>r</i>	$19.09 \pm 0.06$
PS1/ <i>i</i>	$18.49 \pm 0.03$
PS1/ <i>z</i>	$18.21 \pm 0.04$
PS1/ <i>y</i>	$17.93 \pm 0.15$
LS/ <i>g</i>	$19.89 \pm 0.02$
LS/ <i>r</i>	$18.86 \pm 0.01$
LS/ <i>z</i>	$18.01 \pm 0.02$
2MASS/ <i>J</i>	$17.82 \pm 0.18$
2MASS/ <i>H</i>	$16.77 \pm 0.11$
2MASS/ <i>K</i>	$17.00 \pm 0.16$
WISE/ <i>W1</i>	$17.36 \pm 0.04$
WISE/ <i>W2</i>	$17.47 \pm 0.03$

**Notes.** All measurements are in the AB system and are not corrected for reddening.

Table B.2: Host photometry of ZTF20abjyrxf

ZTF20abjyrxf	
SDSS/ <i>u</i>	$21.29 \pm 0.91$
SDSS/ <i>g</i>	$19.99 \pm 0.08$
SDSS/ <i>r</i>	$19.09 \pm 0.06$
SDSS/ <i>i</i>	$18.67 \pm 0.06$
SDSS/ <i>z</i>	$18.24 \pm 0.16$
PS1/ <i>g</i>	$19.92 \pm 0.12$
PS1/ <i>r</i>	$19.22 \pm 0.08$
PS1/ <i>i</i>	$18.72 \pm 0.04$
PS1/ <i>z</i>	$18.46 \pm 0.06$
PS1/ <i>y</i>	$18.24 \pm 0.17$
LS/ <i>g</i>	$19.84 \pm 0.03$
LS/ <i>r</i>	$18.94 \pm 0.03$
LS/ <i>z</i>	$18.32 \pm 0.02$
WISE/ <i>W1</i>	$18.36 \pm 0.06$
WISE/ <i>W2</i>	$18.87 \pm 0.09$

**Notes.** All measurements are in the AB system and are not corrected for reddening.

Table B.3: Host photometry of ZTF21aablrfe

ZTF21aablrfe	
GALEX/ <i>FUV</i>	$23.20 \pm 0.27$
GALEX/ <i>NUV</i>	$22.83 \pm 0.20$
SDSS/ <i>u</i>	$22.33 \pm 0.54$
SDSS/ <i>g</i>	$20.89 \pm 0.09$
SDSS/ <i>r</i>	$19.72 \pm 0.05$
SDSS/ <i>i</i>	$19.16 \pm 0.04$
SDSS/ <i>z</i>	$18.55 \pm 0.07$
PS1/ <i>g</i>	$20.63 \pm 0.14$
PS1/ <i>r</i>	$19.63 \pm 0.06$
PS1/ <i>i</i>	$19.15 \pm 0.04$
PS1/ <i>z</i>	$18.81 \pm 0.04$
PS1/ <i>y</i>	$18.77 \pm 0.16$
LS/ <i>g</i>	$20.61 \pm 0.03$
LS/ <i>r</i>	$19.51 \pm 0.03$
LS/ <i>z</i>	$18.61 \pm 0.02$
2MASS/ <i>J</i>	$18.28 \pm 0.19$
2MASS/ <i>H</i>	$18.03 \pm 0.25$
2MASS/ <i>K</i>	$17.49 \pm 0.13$
WISE/ <i>W1</i>	$17.61 \pm 0.06$
WISE/ <i>W2</i>	$17.73 \pm 0.05$

**Notes.** All measurements are in the AB system and are not corrected for reddening.

Table B.4: Host photometry of ZTF21abcwuhh

ZTF21abcwuhh	
SDSS/ <i>u</i>	20.12 ± 0.30
SDSS/ <i>g</i>	19.40 ± 0.08
SDSS/ <i>r</i>	18.17 ± 0.04
SDSS/ <i>i</i>	17.62 ± 0.04
SDSS/ <i>z</i>	17.07 ± 0.07
PS1/ <i>g</i>	19.65 ± 0.19
PS1/ <i>r</i>	18.22 ± 0.06
PS1/ <i>i</i>	17.62 ± 0.05
PS1/ <i>z</i>	17.39 ± 0.04
PS1/ <i>y</i>	17.11 ± 0.05
LS/ <i>g</i>	19.66 ± 0.08
LS/ <i>r</i>	17.98 ± 0.05
LS/ <i>z</i>	17.28 ± 0.03
2MASS/ <i>H</i>	16.15 ± 0.06
2MASS/ <i>K</i>	16.01 ± 0.06
WISE/ <i>W1</i>	16.81 ± 0.03
WISE/ <i>W2</i>	17.29 ± 0.03

**Notes.** All measurements are in the AB system and are not corrected for reddening.

Table B.7: Host photometry of ZTF22aahmovu

ZTF22aahmovu	
SDSS/ <i>u</i>	21.23 ± 0.35
SDSS/ <i>g</i>	19.56 ± 0.05
SDSS/ <i>r</i>	18.68 ± 0.02
SDSS/ <i>i</i>	18.26 ± 0.03
SDSS/ <i>z</i>	18.00 ± 0.10
PS1/ <i>g</i>	19.64 ± 0.08
PS1/ <i>r</i>	18.74 ± 0.05
PS1/ <i>i</i>	18.27 ± 0.04
PS1/ <i>z</i>	17.98 ± 0.05
PS1/ <i>y</i>	17.79 ± 0.14
LS/ <i>g</i>	19.54 ± 0.02
LS/ <i>r</i>	18.53 ± 0.02
LS/ <i>z</i>	17.87 ± 0.02
2MASS/ <i>J</i>	17.81 ± 0.21
2MASS/ <i>H</i>	17.71 ± 0.32
WISE/ <i>W1</i>	17.65 ± 0.04
WISE/ <i>W2</i>	17.93 ± 0.04

**Notes.** All measurements are in the AB system and are not corrected for reddening.

Table B.5: Host photometry of ZTF22aabifrp

ZTF22aabifrp	
PS1/ <i>g</i>	21.24 ± 0.18
PS1/ <i>r</i>	20.22 ± 0.13
PS1/ <i>i</i>	19.89 ± 0.15
PS1/ <i>z</i>	19.56 ± 0.11
PS1/ <i>y</i>	19.37 ± 0.15
LS/ <i>g</i>	21.04 ± 0.18
LS/ <i>r</i>	20.01 ± 0.14
LS/ <i>z</i>	19.34 ± 0.10
2MASS/ <i>J</i>	18.87 ± 0.40
2MASS/ <i>H</i>	18.08 ± 0.20
2MASS/ <i>K</i>	17.96 ± 0.28

**Notes.** All measurements are in the AB system and are not corrected for reddening.

Table B.6: Host photometry of ZTF22aadeqlh

ZTF22aadeqlh	
GALEX/ <i>FUV</i>	21.96 ± 0.59
GALEX/ <i>NUV</i>	20.53 ± 0.16
SDSS/ <i>u</i>	20.57 ± 0.21
SDSS/ <i>g</i>	19.62 ± 0.03
SDSS/ <i>r</i>	18.84 ± 0.02
SDSS/ <i>i</i>	18.49 ± 0.04
SDSS/ <i>z</i>	18.03 ± 0.09
PS1/ <i>g</i>	19.52 ± 0.05
PS1/ <i>r</i>	18.81 ± 0.03
PS1/ <i>i</i>	18.57 ± 0.03
PS1/ <i>z</i>	18.30 ± 0.06
PS1/ <i>y</i>	18.24 ± 0.06
LS/ <i>g</i>	19.51 ± 0.01
LS/ <i>r</i>	18.67 ± 0.01
LS/ <i>z</i>	18.14 ± 0.02

**Notes.** All measurements are in the AB system and are not corrected for reddening.

Table A.1: Parameters for the 125 candidates that passed the S1 and S2 criteria

ZTF ID	RA (°)	Dec. (°)	Phot. $z$	Peak $M_B$ (phot.)	Ang. sep. (") (phot.)	DESI $z$	Peak $M_B$ (DESI)	Ang. sep. (") (DESI)	SALT2 $x_1$	SALT2 $x_1$ error <sup>1</sup>	SALT2 $c$	SALT2 $c$ error <sup>1</sup>	SALT2 $\chi_r^2$	SALT2 Selection method	Reason for rejection <sup>2</sup>
ZTF19aarfoz*	235.60022	19.58769	0.17	-19.91	0.81	0.18	-20.00	0.87	4.86	0.37	0.07	0.02	2.41	S1	-
ZTF19aatvmug	328.29553	10.48179	0.28	-20.61	0.04	-	-	-	17.06	2.43	0.22	0.04	11.48	S2	a
ZTF19aavocqa	219.56187	10.94207	0.18	-20.50	0.05	-	-	-	-0.54	0.26	0.00	0.02	1.29	S2	b
ZTF19aavrvoc*	209.41258	30.57163	0.22	-20.22	0.06	0.29	-20.87	0.07	10.25	0.85	-0.25	0.02	3.00	S1	-
ZTF19aawtdor	23.58614	30.57753	1.10	-25.74	0.03	-	-	-	17.81	1.97	0.11	0.01	6.53	S2	c
ZTF19aawtdpg	23.76547	30.84236	0.36	-20.52	0.40	-	-	-	13.33	0.58	1.69	0.03	15.39	S2	c
ZTF19aazejcw	16.94976	24.48022	0.16	-20.04	0.26	-	-	-	15.63	1.69	0.34	0.04	20.96	S2	-
ZTF19abamkfs*	323.32348	-10.66276	0.29	-21.22	0.40	-	-	-	6.58	0.66	0.24	0.03	4.43	S2	-
ZTF19abctwkl*	5.08262	10.32489	0.22	-20.07	0.04	-	-	-	15.09	1.00	0.16	0.02	6.19	S2	-
ZTF19abdbshk*	337.5621	-2.3072	0.30	-21.31	2.30	0.28	-21.15	2.23	12.12	0.76	0.09	0.03	6.38	S1	-
ZTF19abdkdze*	20.56833	12.78745	0.18	-20.17	2.39	-	-	-	12.53	0.75	0.36	0.02	13.08	S2	-
ZTF19abfpxuy	326.76663	-3.53944	0.17	-20.64	0.16	-	-	-	8.49	0.37	0.42	0.02	31.22	S2	a
ZTF19abheyzp*	268.14492	13.52266	0.23	-20.80	0.34	-	-	-	-0.29	0.19	0.01	0.02	1.12	S2	-
ZTF19abiptrq	357.1603	19.26281	0.16	-20.08	0.12	-	-	-	10.35	0.35	0.13	0.01	16.22	S2	d
ZTF19abiuibd	246.29544	42.7923	0.27	-21.01	1.53	0.37	-21.71	1.59	12.00	0.60	-0.14	0.01	17.38	S1	e
ZTF19abpfdet*	3.66361	19.74187	0.16	-20.06	0.97	-	-	-	0.44	0.14	0.12	0.01	1.45	S2	-
ZTF19abpjicm*	28.72863	-4.83731	0.24	-20.06	0.87	0.24	-20.00	0.92	2.40	0.62	0.13	0.04	1.04	S1+2	-
ZTF19abqiacu	269.13261	67.98754	0.17	-20.47	0.50	-	-	-	0.26	0.10	0.26	0.01	1.02	S2	b
ZTF19abrbskk	343.58749	-0.60774	0.38	-22.59	0.05	0.50	-23.05	0.19	16.40	1.11	-0.33	0.01	39.16	S1	e
ZTF19abxukuq	23.19197	30.61926	1.11	-24.72	0.05	-	-	-	12.20	1.58	0.05	0.02	5.80	S2	c
ZTF19acbviry	134.92349	11.37289	0.82	-27.19	0.04	-	-	-	0.64	0.33	1.92	0.27	17.85	S2	a
ZTF19acxysdc	205.21535	46.17655	0.16	-19.78	2.34	0.18	-20.10	2.32	5.20	0.08	0.57	0.01	40.25	S1	e,f
ZTF19adbmdsa*	12.87564	24.90057	0.18	-20.11	0.53	-	-	-	-1.31	0.53	0.08	0.05	0.85	S2	-
ZTF20aabqtuv	227.40678	52.54621	0.16	-20.01	0.52	-	-	-	-0.05	0.21	0.07	0.02	1.34	S2	b
ZTF20aafuaj	211.9746	47.87489	0.23	-20.12	0.06	-	-	-	-0.54	0.20	0.03	0.01	1.28	S2	b
ZTF20aahgirj*	260.9763	77.05916	0.17	-20.13	0.75	-	-	-	0.18	0.18	0.10	0.02	1.74	S2	-
ZTF20aahqfra	204.70434	23.38521	1.07	-22.60	0.12	0.53	-21.51	0.12	10.54	0.76	-0.30	0.01	6.09	S1	a
ZTF20aaiqpgv*	148.88927	23.14867	0.29	-20.12	0.69	-	-	-	1.19	0.53	0.07	0.04	1.18	S2	-
ZTF20aandyne	153.92043	17.52974	1.15	-26.00	0.17	0.26	-20.29	0.17	8.42	0.99	-0.04	0.03	1.50	S1	g
ZTF20aarvtor*	256.94862	48.21929	0.30	-20.32	1.14	0.32	-20.56	1.07	10.96	0.37	0.34	0.01	9.52	S1	-
ZTF20aatpirc	140.38973	22.80484	0.18	-20.03	1.97	-	-	-	7.51	1.11	0.15	0.03	1.91	S2	b
ZTF20aatpwrth*	206.97126	30.52111	0.29	-20.60	1.03	0.34	-20.92	1.03	2.37	0.63	-0.21	0.02	0.74	S1	-
ZTF20aaukxvh	281.04003	67.98308	0.19	-19.96	0.43	-	-	-	-	-	-	-	-	S1	h
ZTF20aavvjhr	130.43764	5.54048	0.16	-20.18	0.60	-	-	-	-0.56	0.65	0.12	0.05	0.87	S2	b
ZTF20aawabry*	246.61881	44.58974	0.38	-21.56	1.11	0.29	-20.85	0.94	12.06	0.25	0.13	0.01	14.95	S1	-
ZTF20aawhuut	292.89168	69.31046	0.29	-20.15	2.76	-	-	-	10.03	1.21	0.53	0.04	2.39	S2	e
ZTF20aawfwk*	176.97824	46.48884	0.20	-19.58	0.15	0.31	-20.64	0.17	-2.14	0.24	-0.26	0.03	1.17	S1	-
ZTF20aazpllw	235.85948	41.52658	0.22	-20.74	0.46	0.21	-20.51	0.53	10.47	0.60	1.73	0.09	3.62	S1	i
ZTF20aazyria	216.92081	-7.18886	0.20	-19.84	0.29	0.26	-20.41	0.19	11.34	1.53	0.00	0.05	6.31	S1	a
ZTF20abatizio*	176.16592	68.85701	0.22	-19.91	0.79	0.29	-20.57	0.63	9.45	0.58	0.26	0.02	5.99	S1	-
ZTF20abbudxq	251.03882	25.85802	0.69	-22.42	0.37	0.62	-22.02	0.37	9.40	0.97	-0.01	0.02	3.27	S1	e

Table A.1: continued.

ZTF ID	RA (°)	Dec. (°)	Phot. z	Peak $M_B$ (phot.)	Ang. sep. (") (phot.)	DESI z	Peak $M_B$ (DESI)	Ang. sep. (") (DESI)	SALT2 $x_1^1$	SALT2 $x_1$ error <sup>1</sup>	SALT2 $c^1$	SALT2 $c$ error <sup>1</sup>	SALT2 $\chi_r^2$	SALT2 Selection method	Reason for rejection <sup>2</sup>
ZTF20abeoksh	211.16411	12.81526	0.20	-20.12	0.19	-	-	-	6.34	0.77	0.27	0.04	3.91	S2	a
ZTF20abflhuf*	344.47474	18.42232	0.17	-19.98	1.02	0.22	-20.59	0.96	7.37	0.42	0.01	0.02	3.35	S1	-
ZTF20abgdrea	347.4917	2.06855	0.25	-20.45	0.22	0.25	-20.48	1.73	13.06	2.12	0.03	0.06	3.45	S1+2	j
ZTF20abjyxf*	203.21641	36.97905	0.19	-20.15	0.78	0.22	-20.47	0.76	6.56	0.46	0.13	0.02	3.72	S1+2	-
ZTF20abkdzwb	166.09677	63.71815	0.16	-20.15	0.11	-	-	-	14.25	1.08	0.25	0.02	67.28	S2	a
ZTF20abkwth	217.30394	18.44401	0.27	-20.51	0.56	-	-	-	5.58	0.79	0.01	0.04	6.13	S2	a
ZTF20ablmtxz*	351.52276	15.59055	0.26	-20.26	0.18	-	-	-	-0.88	0.39	0.02	0.05	1.06	S2	-
ZTF20abpntcc	348.95346	1.96946	0.30	-20.53	0.79	-	-	-	11.68	1.11	0.15	0.03	9.31	S2	a
ZTF20abvtvuiq	122.63119	49.23409	0.52	-24.48	0.45	-	-	-	3.63	0.09	0.01	0.01	4.79	S2	c
ZTF20abyffiq	275.77486	55.89199	0.23	-20.21	0.04	-	-	-	18.45	1.06	0.09	0.03	23.79	S2	a
ZTF20abyugxb	269.56948	32.05474	0.27	-19.69	0.11	0.32	-20.22	0.11	10.45	0.63	0.62	0.03	4.75	S1	e
ZTF20aceekkd*	346.6086	-4.24652	0.16	-20.35	0.69	-	-	-	-1.01	0.26	0.03	0.03	0.72	S2	-
ZTF20achldpm	19.72257	9.15695	0.22	-20.35	0.14	-	-	-	-1.17	0.29	0.02	0.04	0.99	S2	b
ZTF20achutix*	71.5033	-22.84677	0.25	-20.55	2.20	-	-	-	14.39	1.09	0.23	0.03	2.22	S2	-
ZTF20acirhoc*	57.20949	-17.91068	0.19	-19.94	1.36	1.37	-26.58	1.34	0.23	0.10	-0.03	0.05	1.20	S1	-
ZTF20acmwssg*	278.85201	74.36068	0.19	-20.33	0.33	0.33	-21.60	0.31	-0.55	0.27	-0.25	0.03	1.45	S1	-
ZTF20acmvzuo*	159.52852	48.50706	0.15	-19.79	1.19	0.18	-20.21	1.14	10.73	0.42	0.49	0.01	78.9	S1	-
ZTF20acotfan*	111.89338	26.65911	0.23	-20.21	0.25	-	-	-	3.14	0.72	0.05	0.05	0.71	S2	-
ZTF20acqhhyr	198.95883	39.92144	0.20	-20.65	0.13	0.18	-20.44	0.13	7.36	0.61	-0.20	0.02	21.65	S1	f
ZTF20acudrme	149.96346	49.28284	0.25	-20.29	2.02	-	-	-	19.72	1.85	0.50	0.02	9.62	S2	e
ZTF20acwyknf	183.08555	6.01879	0.19	-20.15	1.64	-	-	-	-	-	-	-	-	S1	h
ZTF20acxline	110.34336	62.99647	0.19	-20.57	1.35	-	-	-	-	-	-	-	-	S1	h
ZTF20actaxx*	149.88367	15.84733	0.18	-20.24	0.81	0.20	-20.69	0.84	15.35	0.77	0.26	0.01	22.19	S1	-
ZTF20acttdgw	181.31885	42.63599	0.22	-20.09	0.12	-	-	-	14.91	2.12	0.09	0.03	14.51	S2	a
ZTF20acyxxfo	175.83093	12.40494	0.30	-21.64	0.02	0.20	-20.40	0.02	13.64	0.46	0.62	0.01	44.29	S1+2	d
ZTF21aablrfe*	128.64832	44.43092	0.31	-20.35	2.35	0.31	-20.34	2.35	7.66	0.45	0.05	0.02	4.73	S1+2	-
ZTF21aacsvko*	191.87638	60.09603	0.20	-20.25	0.12	0.23	-20.61	0.12	9.02	0.94	-0.06	0.02	7.67	S1	-
ZTF21aahmkzh	182.57745	-1.59476	0.29	-20.77	0.22	0.29	-20.77	0.22	11.01	1.78	-0.05	0.06	3.54	S1	e
ZTF21aamfbcg	197.9838	49.922	0.19	-20.25	0.99	-	-	-	2.26	0.74	0.11	0.05	0.87	S2	b
ZTF21aapreuiq*	179.35798	14.24122	0.23	-21.04	0.43	0.22	-20.93	0.43	-2.35	0.12	-0.28	0.02	1.91	S1	-
ZTF21aarziry	200.54961	-3.32379	0.98	-23.47	1.74	0.93	-23.31	2.24	1.19	0.46	-0.57	0.03	1.91	S1	k
ZTF21aawenoz	278.35686	36.15417	0.19	-20.05	0.29	-	-	-	17.50	0.96	0.24	0.02	23.92	S2	d
ZTF21aawjhse	236.8821	72.33915	0.25	-20.01	0.24	-	-	-	15.01	1.44	0.17	0.03	5.04	S2	a
ZTF21aaxtrsb	227.10148	15.81007	0.18	-20.08	0.05	-	-	-	7.93	0.38	0.16	0.01	8.52	S2	a,e
ZTF21aaxvxbu*	214.55723	-8.57831	0.24	-20.61	0.51	-	-	-	-0.80	0.40	0.38	0.04	1.17	S2	-
ZTF21aaxyiqc	219.99546	66.35707	0.19	-20.03	0.49	-	-	-	0.83	0.35	0.06	0.02	0.99	S2	b
ZTF21abawmyd*	252.85535	62.12331	0.26	-20.31	0.86	-	-	-	-0.80	0.14	0.08	0.02	1.12	S2	-
ZTF21abcwuhh*	232.75625	34.37218	0.34	-20.21	1.55	0.33	-20.17	1.57	3.17	0.75	0.04	0.04	0.99	S1+2	-
ZTF21abcwvhh	229.37915	41.27183	0.32	-20.40	0.67	-	-	-	-	-	-	-	-	S1	h
ZTF21abczvdp	322.84387	18.74866	0.22	-20.06	0.44	-	-	-	0.28	0.44	0.00	0.04	1.27	S2	m
ZTF21abdohu	332.04032	20.11466	0.21	-20.04	0.03	-	-	-	17.59	1.31	0.01	0.02	11.13	S2	a



Table A.1: continued.

ZTF ID	RA (°)	Dec. (°)	Phot. z	Peak $M_B$ (phot.)	Ang. sep. (") (phot.)	DESI z	Peak $M_B$ (DESI)	Ang. sep. (") (DESI)	SALT2 $x_1^1$	SALT2 $x_1^1$ error <sup>1</sup>	SALT2 $c^1$	SALT2 $c^1$ error <sup>1</sup>	SALT2 $\chi_r^2$	SALT2 selection method	Reason for rejection <sup>2</sup>
ZTF21abflhgp	324.87198	-5.24365	0.17	-20.10	0.62	-	-	-	-0.29	0.28	0.03	0.03	1.51	S2	b
ZTF21abfvfa*	249.46712	8.37274	0.32	-20.85	1.84	0.33	-20.93	1.81	2.40	0.30	-0.35	0.02	0.97	S1	-
ZTF21abkqhg	340.58508	-10.26254	0.24	-20.16	0.19	-	-	-	10.36	1.59	0.26	0.06	10.4	S2	a
ZTF21abmwftm	263.21049	33.0329	0.19	-20.22	0.13	-	-	-	14.41	0.43	0.02	0.01	23.64	S2	l
ZTF21abwbemp	351.20487	-13.02944	0.29	-21.09	0.15	-	-	-	7.04	1.93	0.06	0.05	12.50	S2	e
ZTF21abwppie*	257.83269	31.55522	0.19	-20.15	1.06	0.22	-20.42	1.12	5.17	0.22	0.08	0.01	6.66	S1	-
ZTF21abxwlbq	41.83269	-26.44613	0.24	-20.29	0.25	-	-	-	14.14	1.82	0.01	0.04	8.11	S2	a
ZTF21abytadd	209.57168	30.54954	0.23	-20.28	0.23	-	-	-	-1.77	1.55	0.03	0.13	1.06	S2	a
ZTF21abzcoog	45.66843	-25.77305	0.20	-20.7	0.26	-	-	-	13.85	1.41	0.23	0.03	81.55	S2	a
ZTF21acdypeu*	3.11141	17.19754	0.19	-20.10	0.67	-	-	-	0.39	0.25	0.11	0.02	1.27	S2	-
ZTF21aceoae	15.42952	-13.67039	0.17	-20.02	0.17	-	-	-	2.60	0.44	0.17	0.03	1.15	S2	n
ZTF21acujax	126.22946	55.12353	0.17	-20.30	0.13	-	-	-	-	-	-	-	-	S1	h
ZTF21acipntb	133.27407	-7.51718	0.18	-20.06	0.14	-	-	-	12.80	1.45	0.08	0.05	6.49	S2	a
ZTF21acjzszh	121.04104	28.9458	0.29	-20.31	0.16	-	-	-	8.40	1.57	0.04	0.06	3.26	S2	a
ZTF21acmqvwy*	139.62071	56.33775	0.25	-20.06	0.97	-	-	-	-0.26	0.67	0.11	0.03	1.01	S2	-
ZTF22aaaftr	198.20449	-9.0106	0.16	-20.48	0.08	-	-	-	0.42	0.44	0.08	0.03	6.68	S2	b
ZTF22aaayihv	198.20452	-9.01058	0.16	-20.48	0.20	-	-	-	0.41	0.45	0.07	0.03	7.13	S2	b
ZTF22aabfojs*	217.16947	16.92924	0.19	-20.72	0.21	-	-	-	1.67	0.27	0.04	0.02	3.38	S2	-
ZTF22aabifrp*	130.58681	-6.42348	0.25	-21.45	0.14	0.19	-20.94	2.85	5.20	0.97	0.02	0.04	25.30	S1+2	-
ZTF22aabjkis	187.66741	52.40098	0.17	-20.07	0.14	-	-	-	3.00	0.38	0.12	0.03	3.02	S2	b
ZTF22aadephk	199.39315	49.41347	0.19	-20.64	0.30	-	-	-	0.35	0.10	0.09	0.01	2.02	S2	b
ZTF22aadeqlh*	191.8664	64.35601	0.27	-21.11	2.65	0.32	-21.61	2.71	7.51	0.32	0.12	0.01	15.54	S1+2	-
ZTF22aadlpiz	148.79085	26.29379	0.24	-20.26	0.02	-	-	-	6.83	0.75	0.56	0.03	14.75	S2	e
ZTF22aadthbu	118.00643	1.54984	0.19	-20.38	0.80	-	-	-	3.51	0.59	0.08	0.03	4.85	S2	a
ZTF22aafdxdh	195.50497	-3.00991	0.17	-20.01	0.82	-	-	-	-0.37	0.40	0.19	0.04	1.37	S2	b
ZTF22aagdejc	227.98023	2.18405	0.13	-20.15	0.95	1.04	-24.05	0.91	0.91	0.12	-0.56	0.02	3.44	S1	n
ZTF22aaghgma	118.00636	1.54988	0.19	-20.37	0.60	-	-	-	3.54	0.60	0.07	0.03	4.95	S2	a
ZTF22aahhexs	147.15045	23.56611	0.37	-21.26	0.06	0.35	-21.18	0.05	-0.41	0.58	-0.44	0.03	0.92	S1	a
ZTF22aahlry	168.27018	-5.36757	0.19	-20.02	0.32	-	-	-	6.62	1.74	0.32	0.07	6.69	S2	a
ZTF22aahmovu*	234.36278	59.93627	0.22	-20.05	0.58	0.24	-20.34	0.65	9.63	0.66	0.26	0.03	2.19	S1+2	-
ZTF22aakkudf	187.67086	62.42926	0.18	-19.27	2.11	-	-	-	-	-	-	-	-	S1	h
ZTF22aamhyof	197.99237	72.15286	0.20	-20.09	0.22	-	-	-	2.72	0.58	0.09	0.03	1.74	S2	m
ZTF22aamltry*	263.93663	29.36772	0.16	-20.21	1.02	-	-	-	8.63	0.11	0.35	0.01	40.66	S2	-
ZTF22aaoancel	254.0419	54.30948	0.19	-20.39	0.19	-	-	-	2.72	0.10	0.13	0.01	1.8	S2	-
ZTF22aaoelf	245.45402	9.36483	0.16	-20.16	0.97	-	-	-	0.68	0.16	0.03	0.01	1.49	S2	b
ZTF22aaoorkba	324.58735	-0.21367	0.17	-20.11	1.00	-	-	-	-	-	-	-	-	S1	h
ZTF22aaqkvvm*	332.00392	21.20271	0.41	-21.54	2.79	0.37	-21.35	2.81	11.64	0.39	-0.05	0.01	5.60	S1	-
ZTF22aatstmd*	215.36774	38.78523	0.31	-21.08	1.03	0.31	-21.09	2.90	-0.44	0.53	-0.27	0.03	1.10	S1	-
ZTF22aauihjc*	273.50734	50.66143	0.23	-19.99	0.44	0.27	-20.38	0.28	9.23	0.67	0.21	0.03	4.95	S1	-
ZTF22aaavoice	357.17357	-10.54769	0.32	-20.55	0.05	-	-	-	18.27	4.87	0.04	0.06	7.81	S2	a
ZTF22aayumf	41.70816	-8.39824	1.01	-26.99	0.21	-	-	-	18.59	2.89	1.53	0.24	11.04	S2	a

Table A.1: continued.

ZTF ID	RA (°)	Dec. (°)	Phot. $z$	Peak $M_B$ (phot.)	Ang. sep. (") (phot.)	DESI $z$	Peak $M_B$ (DESI)	Ang. sep. (") (DESI)	SALT2 $x_1$	SALT2 $x_1$ error <sup>1</sup>	SALT2 $c$	SALT2 $c$ error <sup>1</sup>	SALT2 $\chi_r^2$	SALT2 selection method	Reason for rejection <sup>2</sup>
ZTF22abakgnp*	257.97571	8.08988	0.25	-20.25	0.62	-	-	-	0.58	0.36	0.04	0.03	1.31	S2	-
ZTF22abcsqha	14.15889	-16.49492	0.25	-20.43	0.30	-	-	-	6.80	0.77	0.13	0.03	19.58	S2	a

\* Objects that passed the visual inspection and are in the final sample.

<sup>1</sup> The SALT2 fit parameters are from the fit with a DESI  $z$ , if available. Otherwise, they are from the fit with a photometric  $z$ .

<sup>2</sup> The reasons for rejection are given as follows:

- (a) Likely AGN/QSO;
- (b) DESI  $z < 0.15$ ;
- (c) Stellar variability;
- (d) Likely a TDE (e.g. due to a dust echo, or light curve decline matching an exponential decay);
- (e) Long duration/rise time, so likely SLSN;
- (f) Bumps in light curve suggest circumstellar interaction;
- (g) Lens galaxy would be too faint (from LS colours);
- (h) Changes in DESI processing meant that the redshift is now too small;
- (i) Issues with ZTF data processing;
- (j) Candidate lens system from SuGOHI VI catalogue (Sonnenfeld et al. 2020), likely lensed QSO;
- (k) More likely associated with closer nearby galaxy (with LS photo.  $z = 0.090 \pm 0.006$ );
- (l) Confirmed TDE (Yao et al. 2022);
- (m) DESI  $z$  available that means  $M_B > -20$  mag;
- (n) Confirmed SN Ia-9IT.